REVIEW

Check for updates

Revitalizing zinc-ion batteries with advanced zinc anode design

Shuwei Chen,†[a] Huibo Wang,†[ab] Mengyu Zhu,[a] Fan You, [iD][a] Wang Lin,[d] Dan Chan,[a] Wanxin Lin,[a] Peng Li,[a] Yuxin Tang [iD] *[ac] and Yanyan Zhang*[a]

Rechargeable aqueous zinc-ion batteries (AZIBs) have attracted significant attention in large-scale energy storage systems due to their unique merits, such as intrinsic safety, low cost, and relatively high theoretical energy density. However, the dilemma of the uncontrollable Zn dendrites, severe hydrogen evolution reaction (HER), and side reactions that occur on the Zn anodes have hindered their commercialization. Herein, a state-of-the-art review of the rational design of highly reversible Zn anodes for high-performance AZIBs is provided. Firstly, the fundamental understanding of Zn deposition, with regard to the nucleation, electro-crystallization, and growth of the Zn nucleus is systematically clarified. Subsequently, a comprehensive survey of the critical factors influencing Zn plating together with the current main challenges is presented. Accordingly, the rational strategies emphasizing structural design, interface engineering, and electrolyte optimization have been summarized and analyzed in detail. Finally, future perspectives on the remaining challenges are recommended, and this review is expected to shed light on the future development of stable Zn anodes toward high-performance AZIBs.

1. Introduction

Rechargeable secondary batteries, as highly efficient and convenient green energy storage devices, provide a promising solution for renewable energy storage. Among the energy storage devices, lithium-ion batteries (LIBs) are the most mature electrochemical energy storage systems with the advantages of high efficiency, convenience, and stability.[1–7] Nonetheless, the predicament of the limited lithium reserves, high preparation cost, safety issues arising from the flammable and explosive organic electrolytes, and environmental concerns are challenging their market dominance. Herein, the exploration of safe and inexpensive aqueous batteries is crucial to the upgradation of the energy storage industry. Aqueous zinc ion batteries (AZIBs) are promising for large-scale energy storage devices because of the abundant Zn metal reserves, environmental friendliness, excellent compatibility with aqueous solutions, low redox potential (-0.76 V *vs.* standard hydrogen electrode, SHE), and high theoretical capacity (820 mA h g^{-1} or 5855 mA h cm^{-3}).[8–14] Although great progress has been made in the research on cathode materials for AZIBs, such as polyanion compounds, manganese dioxide, vanadium

oxide and Prussian blue,[15–17] the notorious bottlenecks such as Zn dendrite growth, hydrogen evolution reaction (HER), and side reactions that occur on the surface of Zn anode severely deteriorate the Coulombic efficiency (CE) and performance of AZIBs, limiting their further commercialization.[18–23] Regarding the Zn dendrites, which probably pierce the separator, cause short-circuit and fall off from the Zn anodes inducing "dead zinc".[24–26] It is known that Zn nucleation thermodynamics depends on the critical nucleation overpotential (η), and a smaller nucleation size would be created with higher η, benefitting the uniform and fine-grained Zn deposition.[27–31] Moreover, the inhomogeneous electric field and Zn^{2+} ion distribution on the surface of the Zn anode would inevitably induce uneven Zn deposition and finally trigger the formation of Zn dendrites under the "tip effect". Hence, a consistent electric field and homogeneous Zn^{2+} ion distribution are required to alleviate and suppress the Zn dendrite formation and growth.[22,32–35] Besides, the HER (0 V *vs.* SHE) taking place during the process of Zn reduction would increase the local concentration of OH$^-$ ions, further accelerating the corrosion and passivation of the Zn anode.[8,9,18,36] In turn, such continuous corrosion would make an even rougher Zn anode surface, promoting the H$_2$ evolution as well as the uneven Zn plating. Therefore, an in-depth investigation and an understanding of these issues should be implemented to achieve an effective remedy for highly stable Zn anodes.

In this review, we aim to provide a concise design strategies for stabilizing Zn anodes. We first interpret the electrochemical deposition processes of Zn in terms of nucleation, ion

[a] *College of Chemical Engineering, Fuzhou University, Fuzhou 350116, P. R. China.*
 E-mail: yxtang@fzu.edu.cn, zyanyan@fzu.edu.cn

[b] *Institute of Applied Physics and Materials Engineering, University of Macau, Macau 999078, P. R. China*

[c] *Qingyuan Innovation Laboratory, Quanzhou 362801, P. R. China*

[d] *Army Logistics Academy, Chongqing 401311, P. R. China*

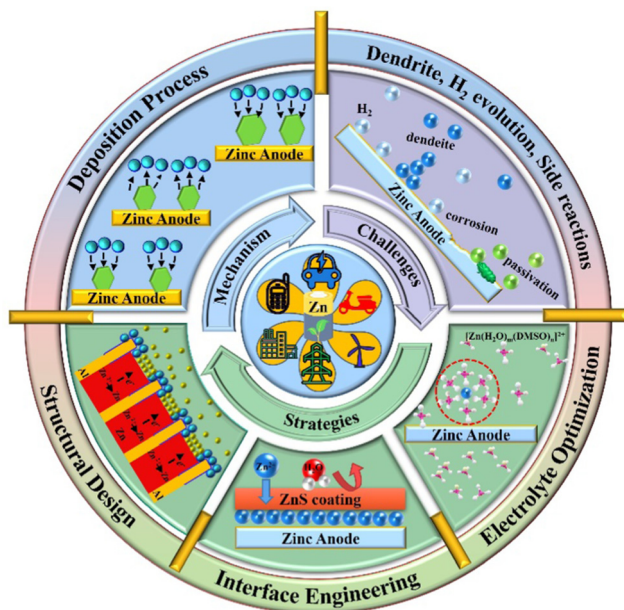† Shuwei Chen and Huibo Wang contributed equally to this work.

Fig. 1 An overview of current challenges and corresponding strategies of AZIBs.

transport, and electro-crystallization. Then, the critical factors that influence Zn deposition, conjugating with the major challenges, are pointed out. Furthermore, the protection strategies are discussed with an emphasis on structural design, interface engineering, and electrolyte optimization, to provide a reasonable design concept for Zn anodes with high stability (Fig. 1). Finally, ourperspectives on future research opportunities targeting the remaining challenges are elaborated to promote the large-scale implementation of AZIBs.

2. Electrochemical deposition of Zn anode

The electrochemical behavior of Zn deposition is essentially composed of the process of Zn^{2+} ion reduction and the electro-crystallization of the newly-born Zn atoms; while the former process follows the thermodynamic rules like the nucleation overpotential, the latter is mainly governed by the electrochemical reaction kinetics involving the diffusion of Zn^{2+} ions and newly-born Zn atoms.[34] Moreover, it is known that the Zn metal electrodeposition is a complex process with several sequential or simultaneous interfacial reaction procedures, including liquid phase mass transfer (migration of Zn^{2+} ions to the electrode surface), pre-transformation (dehydration or rearrangement of hydrated Zn^{2+} ions), charge transfer (Zn^{2+} ions are reduced to adsorbed Zn atoms), and electro-crystallization (adsorbed Zn atoms form crystals by integrating into the lattice or aggregating with other atoms).[20,33,37–39] Since these steps jointly determine the morphology of the deposited Zn layer, a thorough understanding of Zn electrochemical deposition is essential.

In a neutral/mild acidic environment, Zn^{2+} ions normally occur in the hydrated state ($[Zn(H_2O)_6]^{2+}$ ions) and will undergo the so-called desolvation process, where the coordinated water molecules rearrange and further decrease, to be recovered as Zn^{2+} ions during their migration from the electrolyte to the near electrode surface. Subsequently, the transformed Zn^{2+} ions obtain electrons at the interface ($Zn^{2+} + 2e^- \rightarrow Zn$) and then generate unstably adsorbed Zn atoms that can effortlessly migrate over the crystal's surface. Furthermore, the adsorbed Zn atoms migrate to suitable locations (growth points) throughout the surface and undergo a crucial electro-crystallization process including integration into the lattice or aggregation with other newly-born Zn atoms to further grow.[8,40] The detailed electro-crystallization processes can be expressed as follows:

(I) Integration into the lattice. The Zn growth process is related to two basic theories including the epitaxial growth theory and the screw dislocation growth theory. The former refers to the direct growth of nucleating particles into the crystal lattice to achieve the outward extension of the original crystal, while the latter refers to nucleating particles growing at defect sites such as dislocation positions, grain boundaries, and base crystal corners.[41] In actuality, the crystal is imperfect, with multiple kinds of imperfections on its surface, which is more conducive to the growth of screw dislocations. Specifically, the transition from the initial $[Zn(H_2O)_6]^{2+}$ state to the final Zn (kink) state can be achieved through the step-edge ion transfer mechanism and terrace ion transfer mechanism (Fig. 2a), which realize the continuous growth on the original metal lattice.[10,39] The former refers to adsorbed Zn atoms diffusing along the step edges and finally reaching the kink positions. The latter is considered as the process where adsorbed Zn atoms diffuse through the paths with the lowest energy from the flat surface of the terrace region to the step edges, and finally reach kink sites to integrate into the crystals.

(II) Agglomeration and growth. The initially adsorbed Zn atoms tend to form single-atom sites with weak binding energy. To enhance the stability, more Zn atoms would aggregate around these single-atom positions to form an atomic cluster, which can further expand to the mesoporous Zn network (Fig. 2b).[42–44] In this regard, the high-resolution high-angle annular dark-field scanning transmission electron microscopy (HAADF-STEM) images have demonstrated the presence of these three forms during Zn deposition, including single atoms, clusters, and porous networks, as shown in Fig. 2c.

In this process, it was found that the mass transfer process of Zn deposition can be explained by the Nernst–Planck (eqn (1)):[11,45]

$$J_d = -\frac{qCD}{kT}\frac{dV}{dx} - D\frac{dC}{dx} + Cv_x \qquad (1)$$

where J_d, q, C, V, x, v_x, D, k, and T represent diffusion flux, unit charge, concentration, electric potential, distance, convection velocity, diffusion coefficient, Boltzmann constant, and temperature, respectively. For a given system, the Zn plating/stripping process is influenced by three factors, namely, potential
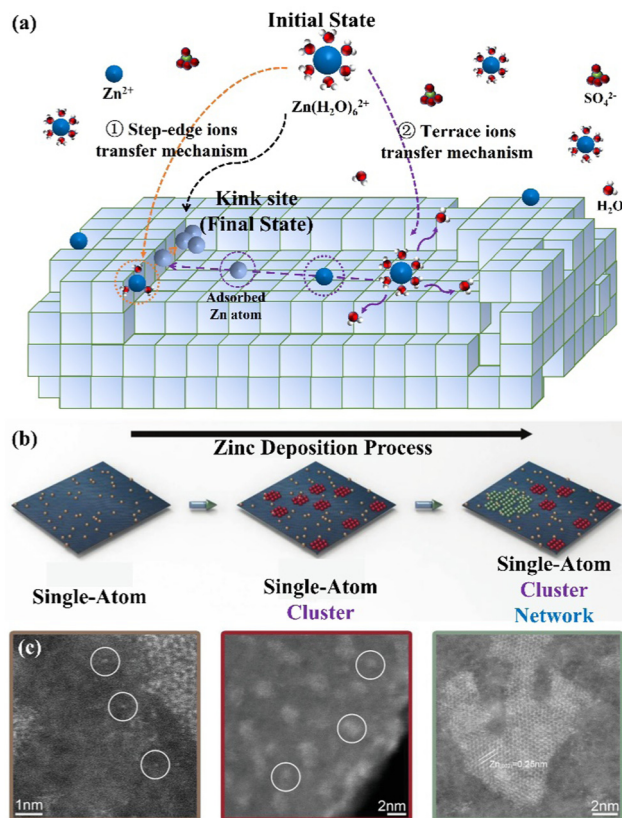
Fig. 2 Schematic diagrams of the (a) step-edge ion transfer mechanism and terrace ion transfer mechanism, and (b) Zn nucleation evolution during deposition: single-atom Zn (brown); Zn cluster (red); Zn porous network (green). (c) The HAADF-STEM images of different forms of Zn atoms on the carbon host. Reproduced with permission from ref. 42. Copyright 2021, Wiley-VCH.

Fig. 3 Schematic diagrams of the finite-difference simulations for (a) Zn^{2+} ions distribution and (b)the electric field under various conditions. Reprinted with permission from ref. 49. Copyright 2020, American Chemical Society. (c) Repeated plating/stripping of Zn at the tip positions. Reproduced with permission from ref. 26. Copyright 2020, Wiley-VCH. (d) A schematic diagram of Zn deposition at the concave edge. Reproduced with permission from ref. 31. Copyright 2021, The Royal Society of Chemistry.

gradient (dV/dx), concentration gradient (dC/dx), and convective velocity (v_x). Convection primarily arises from the concentration gradient, temperature fluctuation, and gas evolution as a result of the HER. Therefore, it is possible to characterize the Zn deposition as a diffusion-controlled process, affected by concentration gradients (refers to ion distribution) and potential gradients (refers to the electric field).[10,11,46,47]

Zn deposition is prone to form a dendritic morphology under the irregular electric field distribution and uneven Zn^{2+} ions distribution near the anode surface. The finite-difference simulations illustrated how the factors like electric field and ion distribution influence the deposition process (Fig. 3a and b).[11,12,48,49] To be more precise, Zn^{2+} ions are adsorbed on the Zn anode's surface before aggregating at the original nucleation sites with 2D-directional diffusion. "Tips" will form since the electric fields at the nucleation sites are substantially stronger than the other sites of the substrate. The sharp tips further exacerbate the irregular electric field and the Zn^{2+} ion concentration polarization on the electrode surface.[20] Finally, vertical Zn deposition and Zn dendrite formation are promoted under the tip effect. (Fig. 3c).[26] The concave edge has a larger electric field as well, which in turn induces the growth of Zn dendrites (Fig. 3d).[31]

Accordingly, electric field and ion distribution significantly affect Zn nucleation and growth. Zn^{2+} ions tend to accumulate in the nucleation sites under a greater electric field, specifically the surface tip and the concave edge of the Zn anode, and then deposit along the vertical direction to form Zn dendrites under the so-called tip effect. Due to the large Young's modulus of Zn ($E_{Zn} \approx 108$ Gpa), the separator will be quickly penetrated by Zn dendrites, which causes an internal short circuit.[9,50]

The plating/stripping curve is an effective tool for studying the process of Zn plating/stripping, which can determine the kinetic and thermodynamic processes of Zn deposition, including Zn nucleation, nuclei growth, Zn stripping and the soft shorts (SS). Firstly, the time–voltage curve (Fig. 4) can accurately reflect the plating/stripping process. In detail, the potential of the working electrode will drop to the nucleation overpotential (η_n) firstly to provide sufficient energy to drive nucleation (Fig. 4a, point i), and then the Zn deposition will occur on the Zn anode. Subsequently, the overpotential decreases because the energy barrier for nuclei growth is less than that for nucleation. Therefore, a rebound (Fig. 4a, curve ii–iii) representing the continued process of nuclei growth is observed.[51,52]

The differences and effects of the initial plating and initial stripping process of the Zn anode have been studied in depth as shown in Fig. 4a and b. It was found that the two different initial processes of plating and stripping have different morphological evolution of zinc metal anode. The initial plating process includes the nucleation stage (Fig. 4a, i) and the growth of nuclei (Fig. 4a, ii–iii), while the initial stripping process
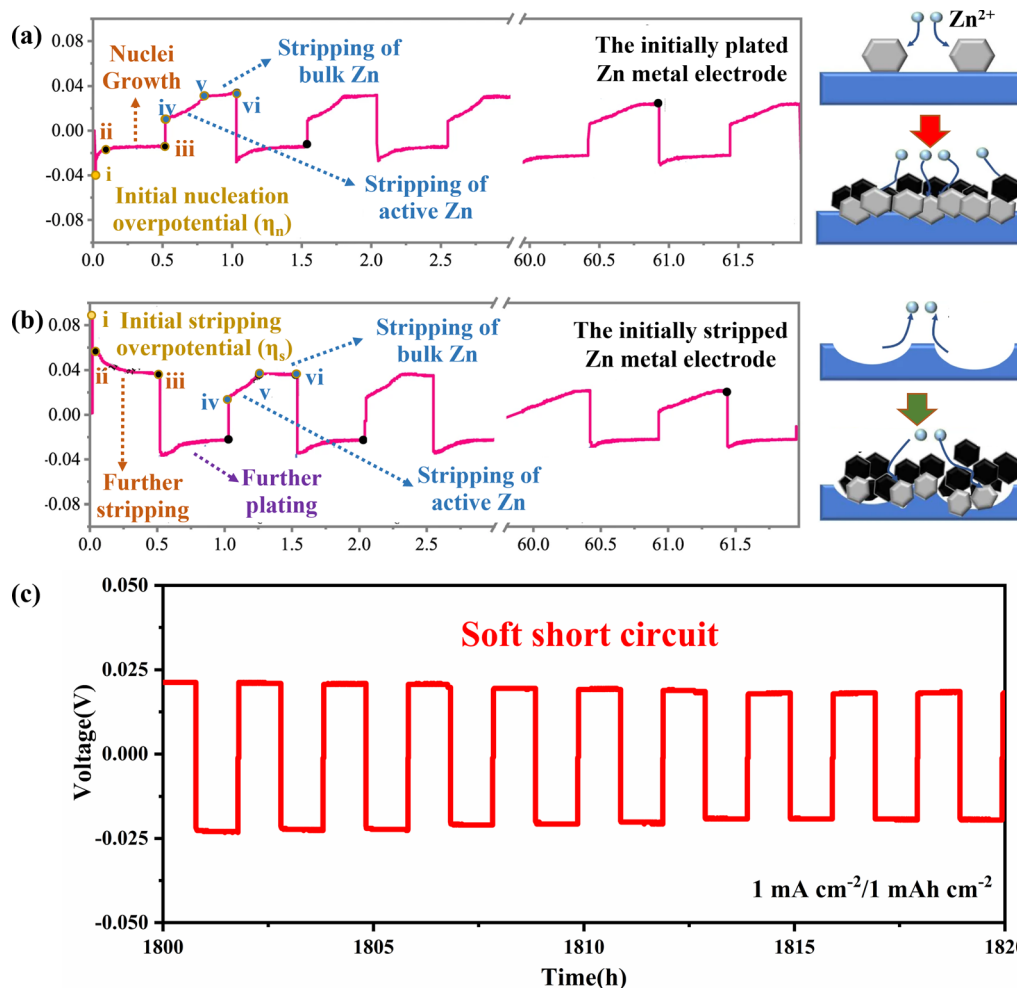
Fig. 4 The time–voltage curves and corresponding schematic diagram of Zn plating/stripping behaviour of (a) P-Zn, and (b) S-Zn. Reproduced with permission from ref. 52. Copyright 2022, Springer Nature. (c) "Soft Short" phenomenon in symmetric cells.

includes the initial stripping of bulk Zn in Zn foil (Fig. 4b, i) and further stripping of Zn at dissolution sites (Fig. 4b, ii–iii). The morphological evolution of the initial Zn plating electrode (P-Zn) and the initial Zn stripping electrode (S-Zn) during the cycling process can be elucidated by combining voltage profiles and *in situ* morphological observations (Fig. 4a and b). During the cycling process, S-Zn first appears concave, and then more Zn dendrites gradually form at the concave position. P-Zn produces shallower pits and less bulk Zn loss during the stripping process, which is more favorable for uniform Zn plating/stripping behavior.[52,53]

It can also be found through the time–voltage curve that the cycle life of symmetric batteries is generally overestimated, and the root cause of this illusion may be the occurrence of SS, as shown in Fig. 4c. SS refers to a localized electrical contact between two electrodes, allowing direct electron transfer and interfacial reactions to coexist. When the overpotential of the symmetrical cell is very low and the voltage curve is very flat, it means that SS may have occurred. In addition, there are two main methods to detect SS: (1) monitoring the impedance difference after low current density and high current density

cycling tests, and (2) comparing the activation energy (E_a) of the dynamic interfacial reaction.[54]

Given the severe destructiveness of dendrites, the comprehensive investigation of the effects of various factors on the Zn electrodeposition process should be strictly executed, providing theoretical guidance for the preparation of Zn anodes with high reversibility.

3. Influential factors on Zn deposition

The dilemma of Zn dendrites, HER, and corrosion has severely obstructed the large-scale application of AZIBs (Fig. 5a).[55–58] In detail, the non-uniform distribution of the electric field and Zn^{2+} ions trigger the inhomogeneous Zn deposition and dendrite growth. Owing to the weak adhesion to the Zn anode, the Zn dendrites are easily detached from the bulk electrode, resulting in "dead zinc". Moreover, from the thermodynamic perspective, the HER would inevitably occur and raise the local concentration of OH^- ions, causing the corrosion and production of inert by-products (*e.g.*, $Zn_4SO_4(OH)_6 \cdot xH_2O$ (ZSH)),
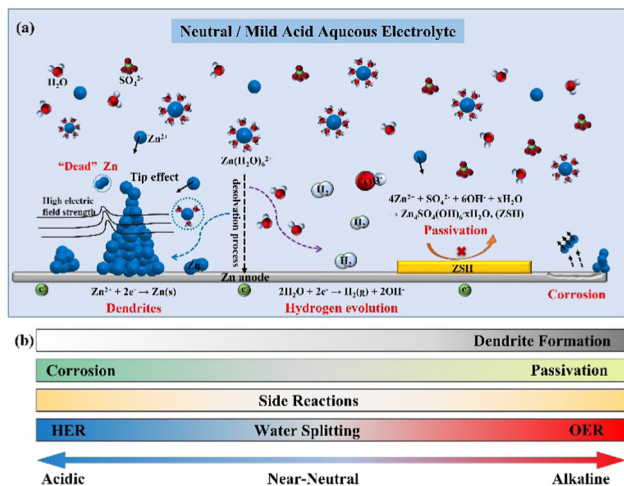
Fig. 5 Schematic diagrams of (a) the mechanism of dendrite growth, HER, and side reactions for the Zn anode; (b) the effect of pH value on zinc anode.

aggravating the interfacial concentration polarization and promoting the growth of Zn dendrites.[26] Since the electro-chemical deposition of Zn is affected and induces morphological changes in the plated Zn, this section will describe in detail the influential factors, such as the pH value of the electrolyte, current density, temperature, and surface morphology and composition, to comprehensively understand the Zn plating processes.
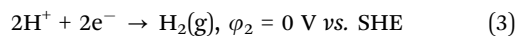
3.1 The effect of the pH of the electrolyte on the deposition process

The stability of the Zn deposition chemistry and the thermodynamic stability of the Zn anode are significantly affected by the pH value of the electrolyte.[33,59] Much effort has been made regarding these studies,[8,33,35,40,60–62] and a thorough explanation should be given about how the pH value of the electrolyte affects the stability of the Zn anode interface.
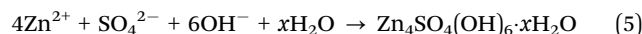
In alkaline electrolytes, Zn^{2+} ions exist in the form of thermodynamically unstable $Zn(OH)_4^{2-}$ ions. When the $Zn(OH)_4^{2-}$ ions reach the limiting concentration, they will be converted into the electrochemically inert byproduct ZnO, resulting in the passivation of the Zn anode.[8,59,63]

While in the neutral/mild acidic electrolyte, the Zn species will present as $[Zn(H_2O)_6]^{2+}$ ions and be reduced to Zn atom by gaining electrons at the electrode surface (Eq. 2, φ_1 is the standard reduction potential of Zn^{2+}/Zn). Moreover, the concomitant HER (Eq. 3, φ_2 is the standard reduction potential of HER) deeply depends on the pH of the electrolyte according to the equation for the H_2 evolution potential (Eq. 4, E_{HER} is the hydrogen evolution overpotential). It is known that the lower the pH value of the electrolyte (the higher the H^+ ion concentration), the more probably the HER will occur.[8] For example, the potential of HER is −0.41 V vs. SHE (neutral environment, pH =7), which is higher than the standard reduction potential of Zn^{2+}/Zn (−0.76 V vs. SHE), indicating that the HER is thermodynamically more favorable.[8,11] Therefore, decreasing

the potential of HER (i.e., increasing the absolute value of E_{HER}) through increasing the pH value is an effective way to reduce H_2 evolution. However, the HER leads to the consumption of H^+ ions in the electrolyte, originating from the decomposition of H_2O molecules, and causes an increase in the local OH^- ions concentration.[64] It is simple to determine that the lower pH value will increase the HER potential based on Eq. (4), which exacerbates the instability of the Zn anode surface. Taking the $ZnSO_4$ electrolyte as an example, as the production of OH^- ions originates from the HER, the electrochemically inert by-product ZSH will be formed when Zn^{2+} ions, SO_4^{2-} ions, and OH^- ions participate in the reaction (5), which leads to the corrosion and passivation of the electrode surface.[65,66] Therefore, the pH value also affects the degree of corrosion and passivation on the Zn anode surface, which drastically limits the reversibility of Zn.

$$Zn^{2+} + 2e^- \rightarrow Zn(s), \quad \varphi_1 = -0.76 \text{ V } vs. \text{ SHE} \quad (2)$$

$$2H^+ + 2e^- \rightarrow H_2(g), \varphi_2 = 0 \text{ V } vs. \text{ SHE} \quad (3)$$

$$E_{HER} = E^\theta - 0.0592 \times pH \ (E^\theta = \text{SHE}) \quad (4)$$

$$4Zn^{2+} + SO_4^{2-} + 6OH^- + xH_2O \rightarrow Zn_4SO_4(OH)_6 \cdot xH_2O \quad (5)$$

The pH value also impacts the side reactions, which in turn affects the formation of Zn dendrites. Corrosion will make an irregular electrode surface and cause uneven electric field distribution, while the presence of a passivation layer hinders the transport of Zn^{2+} ions and intensifies the ion concentration polarization at the interface, thus leading to the generation of Zn dendrites. Dendrites, in turn, expand the area of contact between the electrode and the electrolyte, amplifying the HER even more. The dendrite growth, HER, and side reactions are closely linked and interact with each other.

In conclusion, as the pH value of the solution increases (pH > 7), the solid precipitates (e.g., ZnO and $Zn(OH)_2$) will easily form on the Zn anode, leading to electrode passivation. The thermodynamic stability of Zn decreases as the pH value of the solution decreases (pH < 7), and the hydrogen evolution reactions become easy, causing electrode corrosion and uneven Zn deposition. The formation of a passivation layer will impede the transport of Zn^{2+} ions between the electrode and the electrolyte (Fig. 5b), thus severely affecting Zn deposition and leading to severe dendrites. It is crucial to investigate the appropriate pH value to enhance the stability of the Zn anode.[8,26]

Therefore, selecting an electrolyte solution with a suitable pH value is one of the key factors to guide the uniform and reversible Zn deposition.

3.2 The influence of current density

It has been demonstrated through the simulation results and experimental evidence that the current density plays a significant role in the formation and growth of dendrites during the deposition process.[67,68] Several simulation models, such as the space charge model, the stress-driven dendrite growth model, the nonuniform nucleation model, and the deposition–dissolution

model have been employed to explain the formation and early growth of dendrites. Of these, the space charge model theory has emerged as the most well-acknowledged demonstration.[69,70] Brissot and Chazalviel *et al.*[24,71] revealed that the dendrite growth time "Sand's time (τ_s)" is inversely proportional to the square of the current density, which is described as following:[70,72]

$$\tau_s = \pi D \left(\frac{eC_0Z_c}{2J} \right)^2 \left(\frac{\mu_a + \mu_c}{\mu_a} \right)^2 \qquad (6)$$

where D is the ambipolar diffusion coefficient, C_0 is the initial cation salt concentration, Z_c is the cationic charge number, J is the applied current density, μ_c and μ_a are the cationic and anionic migration numbers, respectively. It is obvious that τ_s is inversely proportional to J^2 (eqn (6)). Therefore, Zn can smoothly deposit under low current density conditions, while a high current density will accelerate the Zn dendrite growth and failure process of short-circuiting for rechargeable ZIBs.[67,68,73]

The nucleation-growth process controlled by nucleation rate (ν_n) and critical radius (r_c) is also closely related to J (eqn (7) and (8)), as shown in Fig. 6a.[72] The ν_n and r_c for the formation of thermodynamically stable nuclei related to the J are as follows:

$$\nu_n \propto \exp\left(-\frac{1}{\log^2 J} \right) \qquad (7)$$

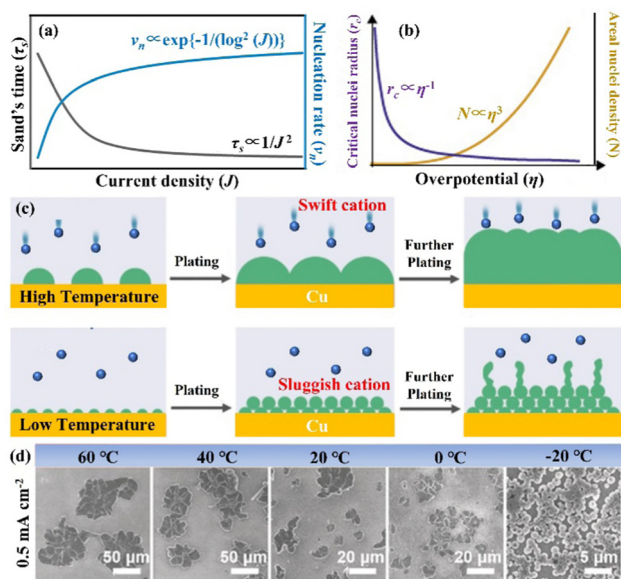$$r_c \propto \frac{1}{|\log J|} \qquad (8)$$

Fig. 6 (a) Theoretical correlation between τ_s/ν_n and J. Reproduced with permission from ref. 72. Copyright 2021, Wiley-VCH. (b) The relationship between the critical nucleation radius, areal nucleation density, and nucleation overpotential. Reproduced with permission from ref. 28. Copyright 2017, American Chemical Society. (c) Schematic diagram of nuclei generation and growth mechanism under high and low temperature. (d) SEM images of nuclei layers under varied temperature conditions. Reproduced with permission from ref. 78. Copyright 2019, Wiley-VCH.

From eqn (7) and (8), it can be concluded that ν_n is proportional to J, while r_c is inversely proportional to J. Therefore, a larger J increases ν_n and decreases r_c as compared to a smaller J. The increased J facilitates more abundant small-size nuclei, which significantly inhibits dendrite growth and achieves dense Zn deposition. These phenomena could be explained by Gibbs free energy and classical nucleation theory where the nucleation and growth of metals are not a spontaneous process and require additional energy to overcome the barriers (nucleation overpotential).[10,12,74] he relationship between the nucleation η and ν_n and r_c are shown in eqn (9) and (10) and Fig. 6b.[11,28,30,72]

$$\nu_n = K \exp\left(\frac{-\pi h \sigma^2 LA}{\rho n FRT\eta} \right) \qquad (9)$$

$$r_c = 2\frac{\gamma V_m}{F|\eta|} \qquad (10)$$

K is the pre-exponential factor, σ is the interfacial tension, n is the valence number of metal ions, T is the absolute temperature, L is Avogadro's number, R and F are the gas constant and Faraday constant, respectively, ρ, A and h are the density, atomic weight and atomic height of the deposited metal Zn, respectively; γ represents the surface energy of the Zn/electrolyte interface and V_m represents the molar volume. This implies that higher η (corresponding to higher J) can provide the extra energy, so Zn can nucleate at locations with higher energy barriers, increasing the number of nucleation seeds with small r_c. Thus, high J can thermodynamically promote uniform and dense Zn deposition.[10,12,28,72]

Based on the above theoretical analysis, the current density (J) affects Zn deposition from two aspects (kinetics and thermodynamics). In terms of kinetics, τ_s is correlated with J. A higher J leads to a shorter τ_s, which increases the growth of Zn dendrites and determines the stability of the Zn anode. Whereas, in thermodynamics, a higher J provides more additional energy for nucleation, which reduces the nucleation radius and increases the nucleation density, contributing to a uniform and dense Zn deposition. Therefore, a rational experimental design is needed to optimize J to balance the kinetically relevant τ_s with the thermodynamically relevant nucleation processes (ν_n and r_c).[72,75,76]

3.3 The influence of temperature

According to previous research, surface free energy between the electrolyte and electrode is strongly dependent on the temperature, where a lower temperature can increase the surface free energy.[77] In addition, the Gibbs free energy of nucleation ΔG is related to the surface free energy as follows:

$$\Delta G = \frac{16\pi\gamma^3 V_m^2 \Phi}{3z^2 e^2 \eta^2} \qquad (11)$$

γ is the surface free energy, V_m is the molar volume of the nucleating atom, Φ reflects the nucleation activity of the substrate, z is the valence of the plating cation, and e is the elementary charge. Since ΔG is independent of T and

approximately constant, the decreased T will increase γ and therefore raise the η value (eqn (11)). According to the eqn (9) and (10), the increased η can increase the ν_n while decreasing the r_c, so the low temperature can induce the nucleation process with a dense deposition. However, the low kinetic process of metal ions at lower temperatures also inhibits the migration of metal ions to the dispersed nucleation sites, which will result in a serious concentration polarization, causing uneven deposition (Fig. 6c and d).[27,72,77–80] In addition, the relationship between temperature and nucleation can be demonstrated by the inhomogeneous plating caused by the inhomogeneous temperature (local high temperature) inside the cell. Therefore, the design of optimized experimental temperatures based on thermodynamic and kinetic analysis can effectively promote the uniform deposition of metals.

3.4 The influence of surface morphology and composition

The surface morphology and composition of the electrode have a tremendous impact on Zn deposition. Zn foil is used as the anode in AZIBs due to its advantages of easy large-scale preparation, however, surface defects such as surface roughness, microcracks, and scratches generated during the manufacturing process can lead to unfavorable factors such as local tip and local stress variations. The so-induced uneven electric field distribution at the electrode/electrolyte interface in turn causes local dendrite growth and a significant decrease in the cycling stability of the Zn anode.[81,82] Fortunately, the polishing process can effectively reduce surface defects and mitigate dendrite growth. Moreover, replacing the planar Zn foil with 3D porous electrodes can also greatly uniformize the charge distribution and interfacial electric field, achieving a dendrite-free anode.[83–85] Besides, it was shown that $Zn_5(CO_3)_2(OH)_6$ and ZnO passivation layers were formed on the surface of Zn metal exposed to air, while this passivation layer hindered the migration and deposition of Zn^{2+} ions on the electrode surface, as well as failed to protect the corrosion of Zn anode in mild acidic electrolytes.[86,87] Therefore, it is essential to add a stable SEI layer to the anode surface. On the other hand, Zn atoms have varied binding energies to different interfaces, and the zincophilic interface with greater binding energy is advantageous to Zn nucleation and guides the orderly growth of Zn.[87–89]

In conclusion, dendrite growth, HER, and side reactions like corrosion and passivation are all interrelated, according to the above analysis. Numerous factors control the formation of Zn dendrites, including the pH of the electrolyte, current density, and temperature, among others. Zn dendrites are only weakly adsorbed to the electrode and may slip away from the bulk electrode during cycling, resulting in "dead Zn" and a reduction in Zn utilization. What's worse, Zn dendrimers with a high young's modulus might penetrate the separator easily, resulting in internal circuit failure. To produce dendrite-free Zn anodes and high-performance AZIBs, it is advantageous to reconstruct a uniform electric field and ion distribution on the electrode surface.[8,9,40] The challenges of HER, corrosion, and passivation also seriously affect the stability of the Zn anode. Accordingly, increasing the HER overpotential of the

Zn anode (in terms of thermodynamic aspects) and reducing the water molecule content/activity on the Zn surface (from kinetic aspects) are the keys to limiting H_2 evolution. Since some metals have a higher HER overpotential than that of Zn, alloyed electrode design is an effective strategy to limit H_2 evolution and enhance corrosion resistance.[33] In addition, the introduction of interfacial coatings or changes in the solventized structure of Zn^{2+} ions can efficiently avoid direct interaction of a large number of active water molecules with the Zn anode, achieving the inhibition of the HER and side reactions.[87]

4. Mitigation strategy

For Zn anodes, the challenges of Zn dendrites, the HER, and side reactions in aqueous electrolytes severely limit the practical application of AZIBs. These problems could be efficiently overcome by controlling the uniform distribution of the electric field and ions, lowering the number of water molecules that are active on the Zn surface, and decreasing the corrosion overpotential and/or increasing the HER overpotential, based on an understanding of the intrinsic failure mechanism. Hence, we have summarized various types of protection strategies in this section, which include electrode structural design, interface engineering, and electrolyte optimization, to achieve high-stability Zn anodes for AZIBs.

4.1 Structure design

The structure design is an efficient technology for obtaining an extremely stable Zn anode. The 3D porous structure greatly increases the contact area between the electrode and electrolyte, reduces the local current density and promotes homogeneous Zn deposition. Additionally, combining Zn metal with metals like Mg, Al, Cu, In, and Ga to create an alloy solid solution can significantly increase the electrode surface's resistance to corrosion. This method optimizes the behavior of Zn deposition and growth as well, resulting in the creation of a fairly reversible Zn anode.

(i) 3D structured Zn anode. The issue of Zn dendrites caused by strong local currents is successfully resolved by designing the 3D porous construction with a large specific surface area.[90,91] Rolison's group[92] reported a 3D sponge structure Zn anode with a high specific surface area, which greatly increased Zn nucleation sites and reduced the local current density on the Zn anode surface, resulting in a uniform and dense Zn deposition (Fig. 7a). This 3D sponge Zn anode effectively solved the problems of passivation and dendrites, and achieved thousands of stable cycles in alkaline nickel–zinc batteries. With the treatment of oxidation, electrodeposition, and high-temperature calcination, Pu's group[84] developed a dual-channel 3D nano-porous Zn anode (denoted as DCP-Zn) for high-speed ion/electron transfer. The DCP-Zn anode's continuous porous conducting skeleton enabled a homogeneous electric field on its surface, and the nano-pores are beneficial for uniform Zn deposition, thereby inhibiting the dendrite growth and
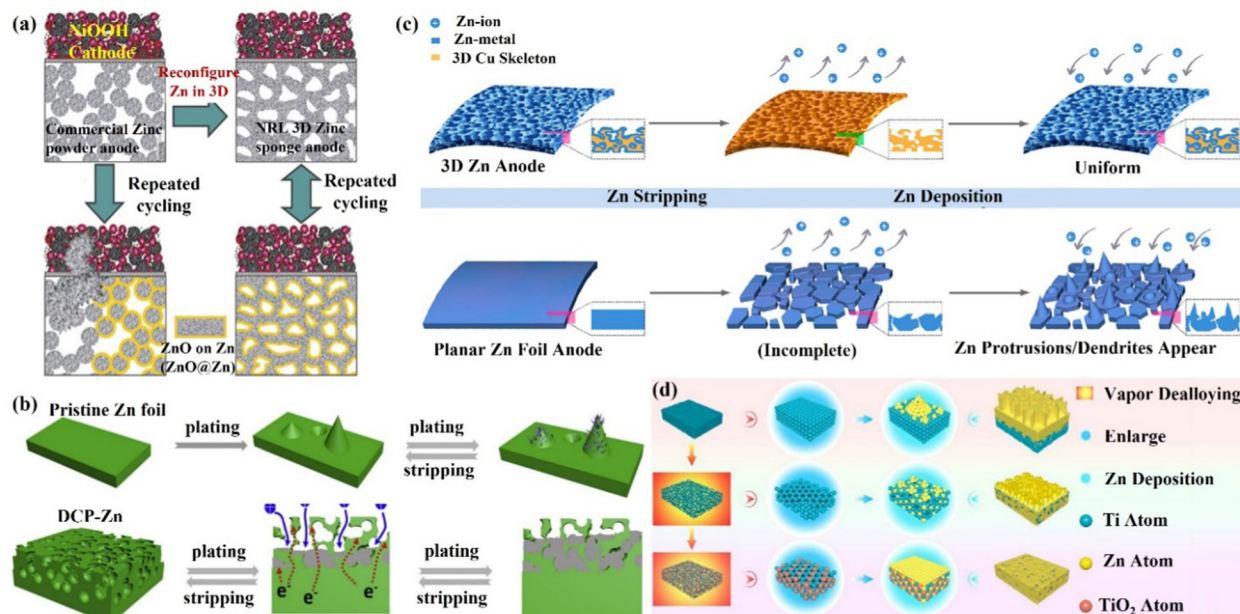
Fig. 7 Schematic diagram of (a) controllable Zn deposition on the designed 3D sponge Zn anode in a Zn–Ni cell. Reproduced with permission from ref. 92. Copyright 2017, The American Association for the Advancement of Science. (b) Repeated Zn plating/stripping behaviors of Zn foil and DCP-Zn. Reproduced with permission from ref. 84. Copyright 2020, Elsevier Inc. (c) The corresponding Zn deposition and stripping process when 3D porous copper skeleton and flat Zn foil are used as electrodes, respectively. Reproduced with permission from ref. 93. Copyright 2019, American Chemical Society. (d) Planar Ti, 3D Ti skeleton, and 3D Ti–TiO$_2$ skeleton as carriers and the corresponding Zn deposition process. Reproduced with permission from ref. 94. Copyright 2021, American Chemical Society.

alleviating the volume variations (Fig. 7b). Moreover, the dual-channel porous structure also facilitated high rates of electron and ion transport, reducing internal polarization and "dead zinc". Ultimately, the DCP-Zn symmetric cell could cycle stably for more than 1400 h and 200 h at 0.1 mA h cm^{-2} and 10 mA h cm^{-2}, respectively, and the DCP-Zn//V$_2$O$_5$ full cell had a high capacity of 443.4 mA h g^{-1} and stable cycling performance (more than 500 cycles). Xu's group[93] reported a 3D porous copper skeleton Zn anode. As a carrier for Zn deposition, the porous copper skeleton possessed strong electrical conductivity and an open architecture that could guarantee uniform Zn deposition. Usually, the Zn foil anode often serves as both the active component and the carrier, which leads to significant volume variations and instability during charging and discharging. The robust and flexible porous copper skeleton can withstand such volume changes, thus improving cycling performance (Fig. 7c). The results showed that the 3D copper skeleton structured Zn anode had stable cycling performance, and the 3D skeleton-Zn//ultrathin MnO$_2$ nanosheet full cell demonstrated good cycling stability with a retained capacity of 173 mA h g^{-1} after 300 cycles at 0.4 A g^{-1}. Qian's group[94] designed 3D porous Ti skeletons and 3D porous Ti–TiO$_2$ skeletons to increase the internal Zn deposition space, limit Zn dendrite formation and mitigate large volume changes.[95,96] As shown in Fig. 7d, the Zn deposition on the porous Ti skeleton was more uniform as compared to that of Zn foil. However, the Zn deposition and growth on the Ti skeleton surface would still lead to the formation of localized sub-micron dendrites due to the weak zincophilicity property of Ti.[97] Therefore, further construction of a porous Ti–TiO$_2$ skeleton

zinc anode with zincophilicity could achieve a long cycle performance of 2000 h, and the 3D Ti–TiO$_2$–Zn/S-Mxene@MnO$_2$ full cell could retain 95.46% of the capacity after 500 cycles at 5 A g^{-1}.

(ii) 3D carbon material skeleton Zn anode. Zincophilic materials can promote nucleation as well as further dense Zn deposition, which can effectively suppress the undesirable effects arising from dendrites. Therefore, the introduction of zincophilic sites can effectively solve the kinetics of Zn deposition. However, issues such as the uneven distribution of zincophilic sites and coverage of zincophilic sites still lead to the failure of this strategy. Chao's group[89] proposed a hierarchical confinement strategy (Fig. 8a) that used zincophilic sites to capture Zn to induce uniform nucleation, and then spatially "enclosed" the subsequently deposited Zn in porous carbon cages and the 3D networks, thus effectively solving the kinetic and stability compatibility problems (Fig. 8b). By combining the zincophobic porous carbon with the zincophilic sites, the direct exposure of the zincophilic sites was prevented to the greatest extent, and the stability of the zincophilic sites was improved while reducing the possibility of water splitting. This structure could also reduce the local current density, and uniform Zn flux, as well as alleviate the volume expansion problem during cycling. In this case, the CoCC-Zn symmetrical cell could maintain stable cycling for more than 800 cycles at 20 mA cm^{-2} (polarization potential of only 65 mV), and the CoCC-Zn//MnO$_2$ full cell achieved a long cycle performance of up to 2000 cycles at 2 A g^{-1}. Li's group[85] prepared a Zn/carbon nanotube (Zn/CNT) foam anode with high conductivity by chemical vapor deposition. During the cycling process, the
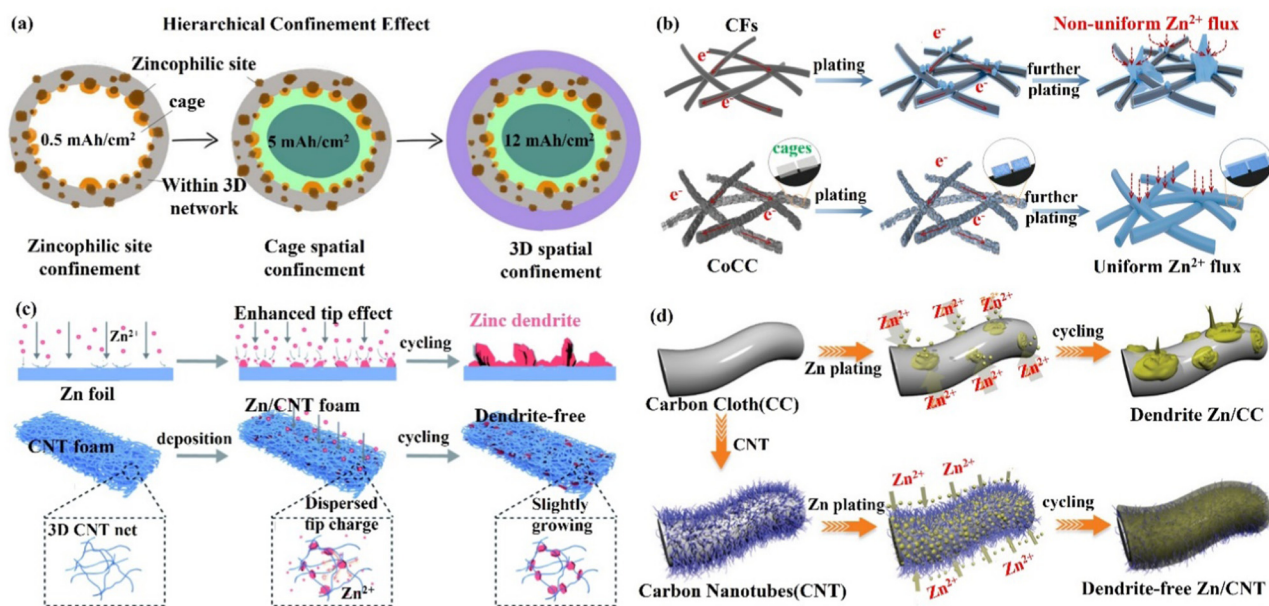
Fig. 8 Schematic diagrams of (a) the hierarchical confinement effect upon Zn deposition, (b) the carbon fiber (CF) skeleton network and the Co-embedded carbon cage (CoCC) skeleton network, which are used as carriers, and the accompanying behaviors of Zn deposition. Reproduced with permission from ref. 89. Copyright 2022, American Chemical Society. (c) Zn dendrite growth on the surface of pristine Zn foil and uniform Zn plating/stripping inside the 3D foam-structured Zn/CNT anode. Reproduced with permission from ref. 85. Copyright 2020, The Royal Society of Chemistry. (d) Zn deposited on carbon cloth (CC) electrode to form dendrites, while on carbon nanotube (CNT) electrode to achieve dendrite-free growth. Reproduced with permission from ref. 98. Copyright 2019, Wiley-VCH.

deposition behavior of Zn occurred mainly inside the carbon nanotube foam network (Fig. 8c), which promoted ion transport and avoided the formation of dendrites. The capacity retention of the Zn/CNT foam symmetric cell remained at 100% after 250 and 100 cycles at 40% and 81% depth of discharge (DOD$_{Zn}$), respectively. The Zn/CNT foam//MnO$_2$ full cell had a long life of up to 10 000 minutes at 3 mA cm^{-2}, and it had outstanding rate performance and stability. With a capacity retention rate of 81.9%, the capacity was 172 mA h g^{-1} after 2500 cycles at 10 C and 83 mA h g^{-1} after 5000 cycles at 30 C. This yields an energy density of 169 W h kg^{-1} and a power density of 3.1 kW kg^{-1}. By integrating a 3D framework (carbon nanotubes, CNT) as a Zn deposition carrier with the substrate of carbon cloth (CC), Lu's group[98] was able to create a high-performance flexible AZIB with good cycling stability by introducing a 3D framework structure of carbon nanotubes (CNT) as a Zn deposition/dissolution carrier. Through this modification, the production of Zn dendrites and by-products was successfully reduced (Fig. 8d). A more homogenous electric field and a significantly smaller Zn nucleation overpotential were obtained by the 3D CNT framework, making the interface more favorable for rapid migration and the uniform nucleation of Zn^{2+} ions.[83,99–102] The Zn/CNT symmetric cell could achieve a stable cycle of 200 h with a CE of 97.9% at a discharge depth of 28%, while the Zn/CNT//MnO$_2$ full cell maintained the capacity retention of 88.7% after 1000 cycles, exhibiting exceptional mechanical flexibility.

(iii) 3D layered anode and alloyed Zn anode. The layered structure and alloyed structure enhance the wettability of the electrode–electrolyte interface, and the high ion transport, and uniform Zn deposition endow the electrode with excellent performance. Qian's group[103,104] constructed a flexible 3D layered Ti$_3$C$_2$Tx MXene@Zn paper as the electrode body, which had high electrical conductivity (15 000 S cm^{-1}), good wettability, and great toughness.[105,106] The layered structure, as illustrated in Fig. 9a, would provide fast electron/ion migration channels; the high surface area and internal space could accomplish uniform charge distribution and prevent the formation of dendrites. Liu's group[107] produced a Zn–Ag alloy electrode by using Zn-soluble metallic silver as a seed material on a carbon substrate to build an alloy solid solution surface layer (Zn$_x$Ag$_{1-x}$) for heterogeneous seed growth and homogeneous Zn deposition (Fig. 9b), and for the first time, used optical microscopy to examine the deposition process of the Zn seed crystals. The majority of Zn was deposited on the silver seeds, which made Zn nucleation and growth more easily regulated in space. Furthermore, Zn^{2+}/Zn$_x$Ag$_{1-x}$ had a greater redox electrochemical potential than Zn^{2+}/Zn, which improved the corrosion resistance of the Zn–Ag alloy anode. Ultimately, the introduction of metallic silver seeds greatly improved the stability of the Zn–Ag alloy electrode.

Yang's group[19] created a 3D nanostructured Zn–Mn alloy anode that could withstand thousands of cycles even under extreme electrochemical conditions. The Zn–Mn alloy (Zn$_3$Mn) electrode had a cauliflower-like microscopic appearance with a large number of internal pores and a super-hydrophilic surface that allowed for mass transfer and homogeneous deposition (Fig. 9c). Atomic force microscopy (AFM), simulation,

Fig. 9 Schematic diagram of (a) the preparation process of the Ti$_3$C$_2$T$_x$ MXene@Zn electrode and its layered structure with fast electron/ion transport channels to promote a uniform Zn deposition process. Reproduced with permission from ref. 103. Copyright 2019, American Chemical Society. (b) Metallic silver as crystalline seed material to construct an alloy solid solution surface layer (Zn$_x$Ag$_{1-x}$) for homogeneous Zn deposition. Reproduced with permission from ref. 107. Copyright 2021, American Chemical Society. (c) Zn deposition at the tip position on the Zn foil anode to form dendrites (top), while it occurs at the grooves and internal nano-pores on the Zn–Mn alloy electrode (bottom). Reproduced with permission from ref. 19. Copyright 2021, Springer Nature. (d) The eutectic Zn–Al alloy anode guiding uniform Zn deposition. Reproduced with permission from ref. 109. Copyright 2020, Springer Nature.

and *in situ* optical microscopy demonstrated that Zn deposition occurred in internal nanopores and grooves between Zn/Mn particles, effectively inhibiting dendrite growth.[108] In addition, the 3D Zn–Mn nanoalloy anode was found to have high corrosion resistance, supporting more than 1000 h of stable charge/discharge cycle performance even under seawater electrolyte and high current density (80 mA cm^{-2}). Jiang's group[109] designed a Zn–Al alloy (Zn$_{88}$Al$_{12}$) anode with an alternating Zn and Al lamellar nanostructure (layer spacing of roughly 450 nm). The Al layer acted as a two-dimensional skeleton capable of generating Al$_2$O$_3$ with insulating properties *in situ*, forming an Al/Al$_2$O$_3$ core/shell structure.[110] When Zn^{2+} ions come in contact with the Al skeleton, Zn^{2+} ions are repelled and fall uniformly between the layers of the Al skeleton due to the electrostatic shielding effect of the Al/Al$_2$O$_3$ layer, thus leading to uniform Zn deposition (Fig. 9d). The presence of Al$_2$O$_3$ also prevents the dissolution of the Al layer and the generation of various by-products, which significantly improves the performance of the Zn–Al alloy electrode.

4.2 Interface engineering

Interface engineering is one of the most important ways to solve the poor stability of Zn anode electrodes. The stability on the electrode–electrolyte interface can be significantly improved by constructing functional material coatings, such as inorganic-, organic- and organic/inorganic hybrid coatings on the surface of the Zn anode. Functional coatings address the

challenges facing Zn anodes by (1) improving the interfacial wettability to make the Zn^{2+} ion flux distribution uniform; (2) avoiding direct contact between electrodes and the electrolyte to inhibit the HER and side reactions on the Zn anode; (3) inducing uniform and dense Zn deposition to effectively extend the cycle life of Zn anodes.

4.2.1 Inorganic coating. (i) Inorganic oxide coating. Inorganic non-metallic materials have been widely used as Zn anode coating materials because of their stable performance, high corrosion resistance, good environmental friendliness, and low cost. Inorganic coatings could limit the two-dimensional diffusion of Zn^{2+} and induce the uniform deposition of Zn^{2+} ions through domain-limiting effects. Zhu's group[88] reported a porous nano-CaCO$_3$ coating that could be applied to the Zn anode surface as a buffering layer to guide the orderly and selective electrodeposition of Zn at the nano-CaCO$_3$ layer/Zn foil interface. This kind of Zn deposition behavior was mainly attributed to the insulating properties and porous structure of the nano-CaCO$_3$ layer. The porous structure was capable of guiding a relatively uniform electrolyte flux on the Zn foil surface, while also allowing Zn^{2+} enrichment at the CaCO$_3$/Zn foil interlayer. The electrically insulating property of CaCO$_3$ allows Zn deposition to occur only on the surface of the Zn foil, forming a CaCO$_3$/Zn microchip/Zn foil trilayer structure (Fig. 10a). Finally, CaCO$_3$@Zn symmetric cells could have their cycle performance increased by a factor of more than 15. Montmorillonite (MMT) has a natural lamellar structure and interlayer cation mobility properties. Li's group[111]
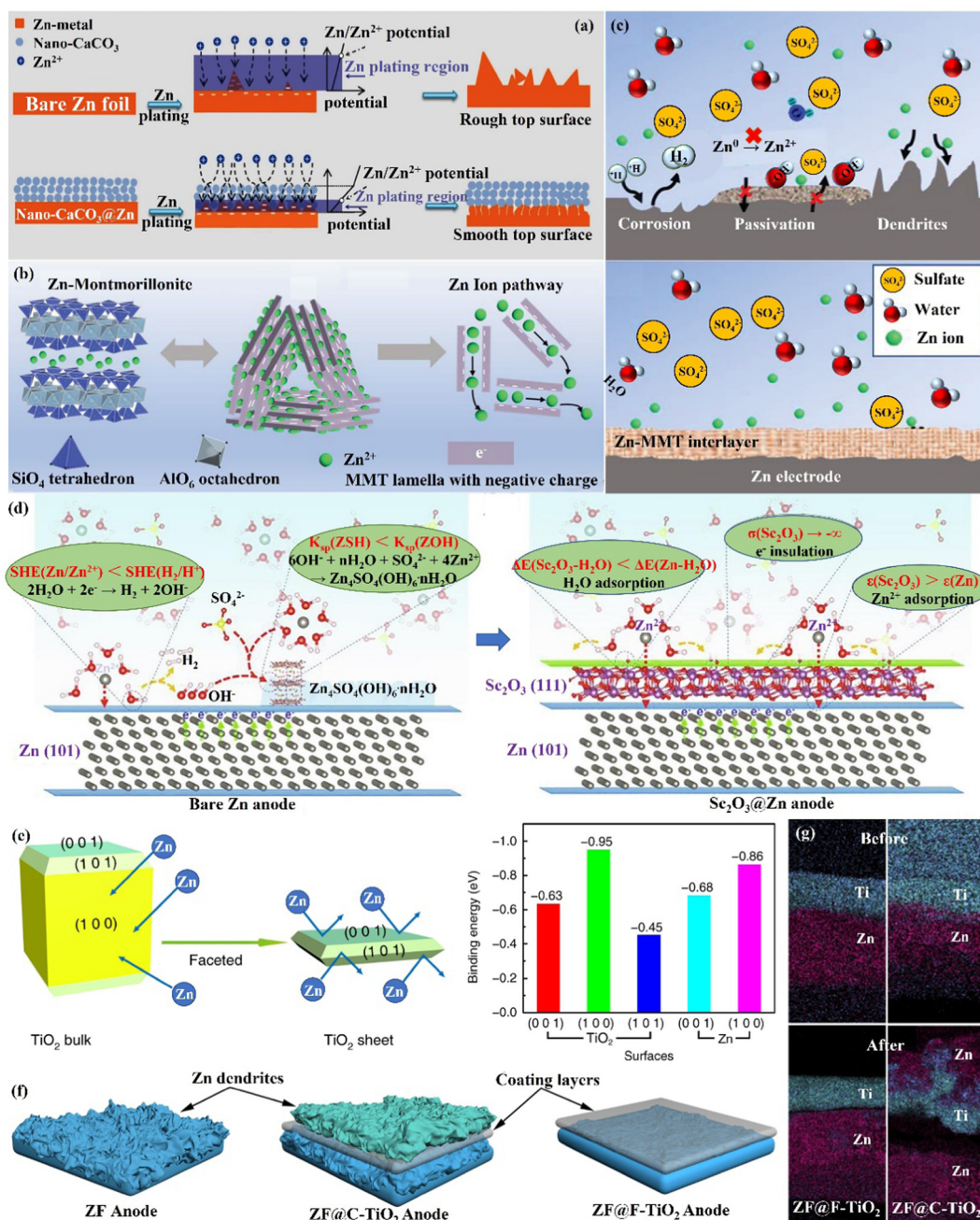
Fig. 10 Schematic diagrams of (a) morphological changes in bare Zn and nano-CaCO₃@Zn anode surfaces during Zn deposition, and the corresponding mechanisms. Reproduced with permission from ref. 88. Copyright 2018, Wiley-VCH. (b) Crystal structure of Zn-based MMT, the charge distribution in MMT lamella, and the interlamellar pathway for Zn^{2+} ion migration. (c) The Zn-based MMT layer promotes uniform deposition while suppressing severe side reactions. Reproduced with permission from ref. 111. Copyright 2021, Wiley-VCH. (d) The modification mechanism of the Zn anode by Sc_2O_3 coating. Reproduced with permission from ref. 65. Copyright 2021, Elsevier Inc. (e) The Calculated Zn atom binding energies with various TiO_2 facets. (f) The behavior of Zn deposition in the presence of various TiO_2 layers. (g) The EDS mapping images of $F-TiO_2$@Zn and $C-TiO_2$@Zn before and after 10 cycles. Reproduced with permission from ref. 112. Copyright 2020, Springer Nature.

obtained zinc-based montmorillonite (Zn-MMT) by ion exchange and constructed it as an artificial SEI for the fast conductivity of Zn^{2+} ions. The MMT crystal was composed of two layers of silica tetrahedron sandwiched by an alumina octahedral layer. When some Al^{3+} ions were replaced by Mg^{2+} ions, a negatively charged sheet interface could be generated. The negatively charged MMT

layer not only enabled fast cation migration ($t_+ \approx 0.82$) and reduced the ion diffusion path, but also ensured sufficient Zn^{2+} ion concentration on the Zn anode surface, which facilitated fast and uniform Zn deposition (Fig. 9b and c). Moreover, the MMT coating material could effectively alleviate the Mn dissolution problem faced by MnO_2 as well. The MMT@Zn symmetric cell

could maintain a stable performance of 1000 cycles at 1 mA cm^{-2}/0.25 mA h cm^{-2} with an overpotential of 50 mV, and even under extreme conditions (10 mA cm^{-2}/45 mA h cm^{-2} with 77% DoD), a consistent cycle of more than 1000 h and an overpotential of only 100 mV could be achieved. The MMT@Zn//MMT-MnO$_2$ full cell was able to perform more than 1100 cycles at 2C and had a capacity of 191.5 mA g^{-1}. The contact between the Zn anode and electrolyte leads to the decomposition of water molecules, causing HER and various side reactions, which is one of the major contributing elements to the instability of the Zn anode. Liang's group[65] reported a hydrophobic multi-channel Sc$_2$O$_3$ protective layer for inhibiting the severe HER. The Sc$_2$O$_3$ coating with layered adsorption not only provided a physical barrier for the Zn anode but also formed hydrogen bonds with H$_2$O molecules (facilitating the desolvation process of [Zn(H$_2$O)$_6$]$^{2+}$ ions). The poor electronic conductivity of the Sc$_2$O$_3$ coating also inhibited the decomposition of active water molecules by gaining electrons, which stifled the factors causing interface instability from the source. Furthermore, the Maxwell-Wagner polarization brought on by the substantial discrepancy between the dielectric constant (ε) of Zn and Sc^{3+} facilitated the diffusion of Zn^{2+} ions and provided more sites for the nucleation of Zn (Fig. 9d). Based on these synergistic effects, the Sc$_2$O$_3$@Zn symmetric cell could cycle stably for more than 100 cycles and maintain a CE of 99.85%. Wang's group[112] prepared TiO$_2$ with a (001) crystalline surface and low zincophilicity as a protective layer, which successfully alleviated the dendrite growth problem and greatly improved the cycle life of the Zn anodes. The binding energy between TiO$_2$ (100) (noted as C-TiO$_2$) and Zn atoms was larger (-0.95 eV) as compared to that of Zn foil, so Zn preferred to be deposited on the highly zincophilic C-TiO$_2$ when C-TiO$_2$ was used as the surface coating. However, the C-TiO$_2$ coating would be covered by Zn deposition after several cycles, resulting in the failure of the protection mechanism. Therefore, TiO$_2$ (001) and (101) with low zinc affinity were further designed (denoted as F-TiO$_2$, Fig. 9e). F-TiO$_2$ had better hydrophilicity, which facilitated the electrolyte penetration and uniform Zn^{2+} ion distribution at the interface.[113] When Zn^{2+} ions migrated to the F-TiO$_2$@Zn anode, Zn^{2+} ions were repelled by the F-TiO$_2$ layer, which led to the enrichment of Zn^{2+} ions at the F-TiO$_2$/Zn interface, and further activated more Zn deposition sites and achieved uniform interlayer lateral Zn deposition sites (Fig. 9f and g). With this protective layer strategy, the F-TiO$_2$@Zn anode symmetric cell could run steadily for more than 460 h at 1 mA cm^{-2}/1 mA h cm^{-2}, outperforming the C-TiO$_2$-Zn anode (190 h) and Zn anode (20 h).

(ii) Zn compound coating. By introducing inorganic elements (S, P, F, O, *etc.*) to form a zinc compound coating with Zn, the charge distribution at the interface could be significantly changed, and the diffusion of Zn^{2+} ions could be promoted to alleviate the concentration polarization on the electrode surface. Guo's group[86] formed a dense artificial SEI layer (ZnS) *in situ* with high mechanical strength, high stability, high adhesion, and high ion diffusion rate on the Zn foil surface by a vapor–solid strategy (Fig. 10a). Due to charge

migration, S atoms formed Zn–S polar bonds with Zn atoms, which enhanced the adhesion of the ZnS layer to Zn foil. The unbalanced charge distribution also facilitated Zn^{2+} ion diffusion between the ZnS and Zn phases, resulting in a high ionic conductivity ($t_{Zn^{2+},ZnS@Zn} = \sim 0.78$ *vs.* $t_{Zn^{2+},Zn} = \sim 0.33$). The ZnS protective layer acted as a physical barrier, isolating the Zn foil anode from direct contact with the electrolyte, and guiding a uniform interlayer plating/stripping process through its insulating property (Fig. 10b). The ZnS@Zn symmetric cell exhibited a life higher than 1100 h at 2 mA h cm^{-1}, and the ZnS@Zn//MnO$_2$ full cell achieved high cycle stability (>2500 cycles) and high coulombic efficiency ($>99.8\%$). Lee's group[114] prepared a new type of zinc metal electrode with controllable surface composition and morphology by a periodic anodization technique, which was denoted as a zinc hexagonal pyramid array electrode coated with a functionalized ZnO layer (ZnO@Zn HPA). The current supply and interruption processes were repeated in a constant cycle to dissolve ZnO in NH$_4$Cl/H$_2$O$_2$ solution and deposit it on the electrode, resulting in the formation of the ZnO coating (Fig. 11c). Through experimental optimization, the best performance of the ZnO@Zn HPA electrode was determined when the "splitting" value was 2 (*i.e.*, the ratio of current disconnection time to current on time was 2). HPA increased the specific surface area, which reduced the local current density and facilitated the uniform distribution of Zn^{2+} ions. the functionalized ZnO passivation layer had a gradient thickness (thicker at the top than at the edges and bottom, with higher interfacial resistance), which could guide the deposition of Zn on the sides and bottom (Fig. 11c and d). After 1000 cycles at 9.0 A g^{-1} (29.22C), the ZnO@Zn//MnO$_2$ full cell continued to operate excellently, with the CE remaining above 99%. Yang's group[115] prepared a Zn–P solid solution alloy coating with corrosion resistance by electrochemical deposition. The ZnP layer was able to maintain a certain electrochemical activity and capacity contribution, which was beneficial for enhancing the energy density. The addition of P atoms significantly increased the binding energy with Zn atoms (Fig. 11e), which promoted the transfer and deposition of Zn^{2+} ions. The ZnP@Zn symmetric cell was cycled for over 300 h at 20 mA cm^{-2}/30 mA h cm^{-2}, and the ZnP@Zn//MnO$_2$ full cell still had a discharge-specific capacity of 154.4 mA h g^{-1} after 1000 cycles at 1 A g^{-1}. A 3D interconnected ZnF$_2$ matrix was created by Yang's group[116] to serve as a multipurpose protective layer (Fig. 11f), which redistributed the Zn^{2+} ion flux and was able to significantly reduce the activation energy of [Zn(H$_2$O)$_6$]$^{2+}$ desolvation, resulting in more stable Zn deposition kinetics. The ZnF$_2$ layer also allowed the insertion of Zn^{2+} ions and induced uniform Zn deposition behavior under the layer through an interstitial diffusion mechanism, which inhibited the growth of dendrites.[117–120] Moreover, the properties of ZnF$_2$ coating such as corrosion resistance, inhibition of HER, and better wetting made the ZnF$_2$@Zn anode more stable. A ZnF$_2$@Zn symmetric cell was obtained with a long cycle duration of 800 h and a high CE of 99.5%. The ZnF$_2$@Zn//V$_2$O$_5$ full cell was stabilized at 279.2 mA h g^{-1} after 2000 cycles at 10 A g^{-1}, with a capacity retention rate of 96%.
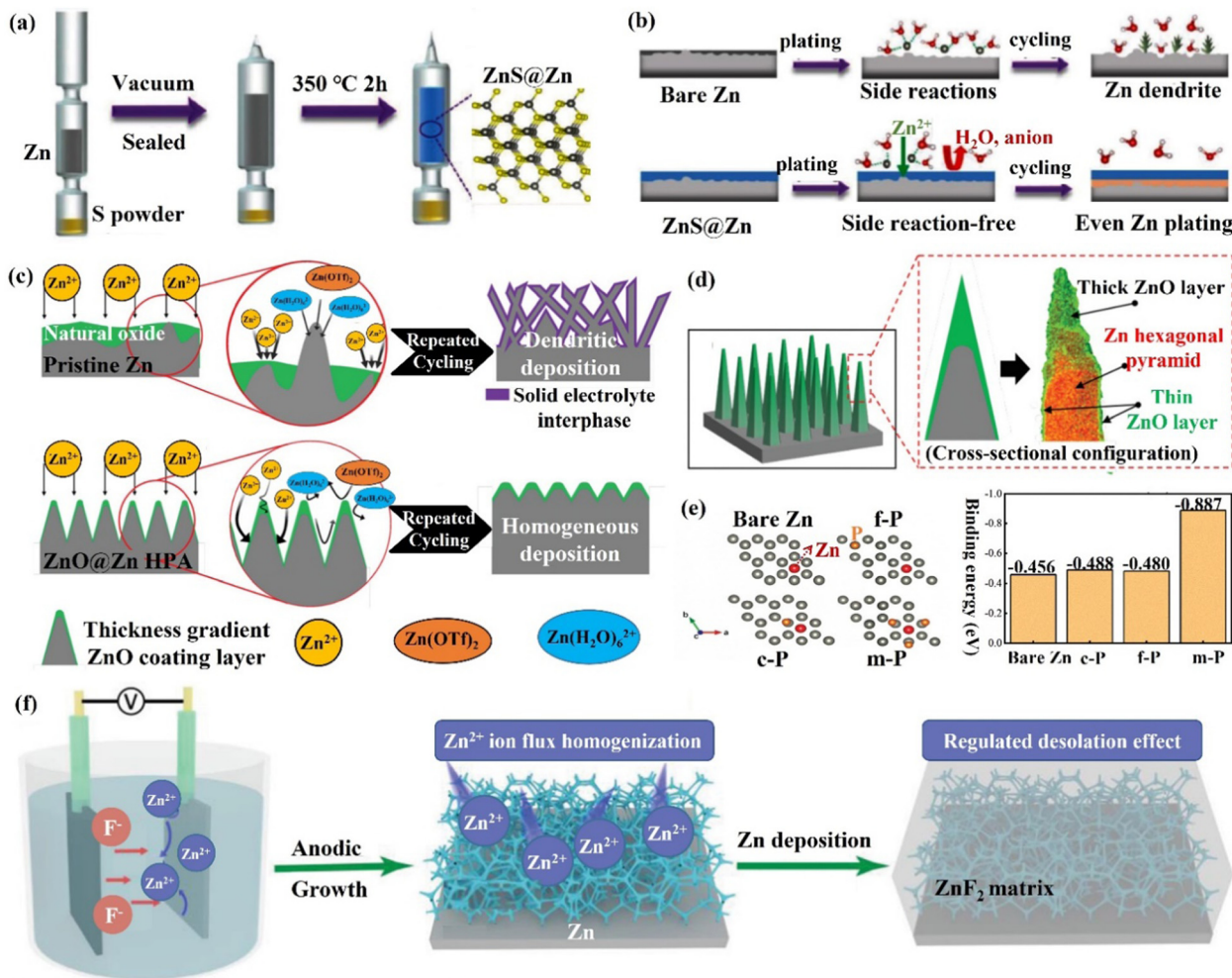
Fig. 11 Schematic diagrams of (a) an *in situ* method for adding the ZnS layer to the Zn metal substrate, (b) Zn deposition behavior with/without ZnS layer. Reproduced with permission from ref. 86. Copyright 2020, Wiley-VCH. (c) Zn deposited on a pristine Zn anode and the ZnO@Zn HPA anode, (d) the cross-sectional configuration of the dendrite-free "functionalized ZnO layer" coated on a Zn HPA. Reproduced with permission from ref. 114. Copyright 2020, Wiley-VCH. (e) Zn was adsorbed on the bare Zn and ZnP layer at different adsorption sites, and the corresponding binding energy was calculated by the DFT. Reproduced with permission from ref. 115. Copyright 2021, Wiley-VCH. (f) The fabrication of the ZnF_2@Zn anode and corresponding Zn deposition behavior. Reproduced with permission from ref. 116. Copyright 2021, Wiley-VCH.

(iii) Metal coating. Metallic materials have recently been widely used in Zn anode interface modification strategies due to their high electrical conductivity and low impact on the battery as an anode surface coating. Tu's group[121] formed a strong metallic tin (Sn) coating on the surface of Zn by chemical vapor deposition, which effectively inhibited the HER and corrosion.[122,123] Moreover, the Sn nanoparticles formed on the Sn coating could also guide the uniform deposition of Zn^{2+} ions and avoid the formation of dendrites. With this modification, the Sn@Zn symmetric cell could cycle steadily for more than 500 h. Yang's group[18,124] coated a layer of indium metal (In) with dual functions of corrosion inhibitor and nucleation agent to achieve the simultaneous inhibition of corrosion and dendritic problems at the Zn anode (Fig. 12a). In had zincophilicity, and the adsorption energy of In to Zn atoms was higher than that of Zn foil, making Zn^{2+} ions preferentially deposited on the In substrate.[125] Moreover, the

higher roughness and specific surface area of the In layer led to lower current density and uniform Zn^{2+} ion flux for uniform Zn deposition. The In@Zn symmetric cell could then achieve a stable cycle of 1500 h with a polarization voltage of 54 mV. Furthermore, Ji's group[126] and Zhang's group[127] were inspired by the gallium–indium–zinc phase diagram to design electrochemically inert gallium–indium (Ga–In) liquid alloy coatings, which effectively suppressed corrosion, HER and dendrite growth under the synergistic liquid alloying-diffusion strategy. The liquid Ga–In alloy had high zincophilicity and high charge conductivity. When the liquid Ga–In surface was newly generated with Zn atoms, the Zn atoms rapidly diffused into the Ga–In alloy interlayer through the zincation of the binary alloy phase. Once the Zn ratio exceeded the limit of the solid phase line of the alloy, the excess Zn atoms spontaneously grew inward and quickly "sank" into the liquid intermediate layer, and then nucleated uniformly near the Zn foil side (Fig. 12b).
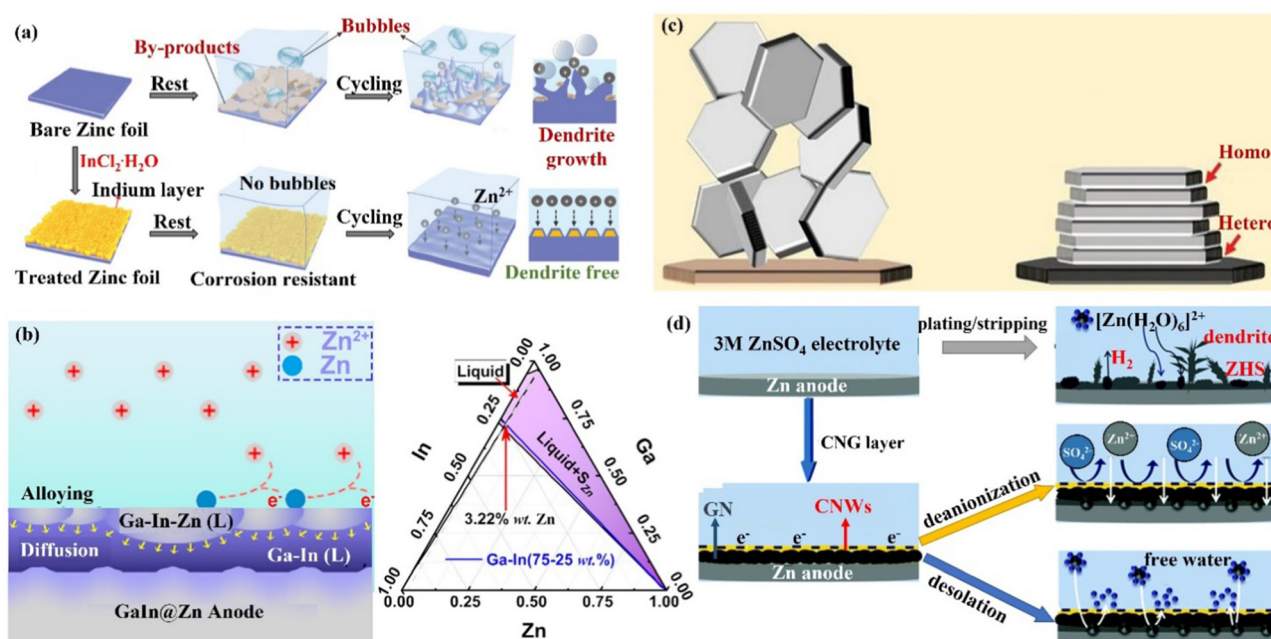
Fig. 12 A schematic diagram of (a) Zn deposition on bare Zn and In@Zn anode. Reproduced with permission from ref. 18. Copyright 2020, Wiley-VCH. (b) The Ga–In–Zn phase diagram, and alloying-diffusion mechanism for dendrite-free Zn deposition. Reproduced with permission from ref. 126. Copyright 2021, American Chemical Society. (c) Using graphene (002) as a substrate to achieve the epitaxial deposition of Zn. Reproduced with permission from ref. 133. Copyright 2019, The American Association for the Advancement of Science. (d) Zn deposition behavior in the presence/absence of CNG film. Reproduced with permission from ref. 134. Copyright 2021, The Royal Society of Chemistry.

The stability of the Zn anode was significantly increased by the liquid Ga–In alloy coating, and the Ga–In@Zn symmetric cell was able to cycle steadily for more than 2100 h at 0.25 mA cm^{-2} with a polarization voltage of just 24 mV, and the Ga–In@Zn//MnO$_2$ full cell was cycled more than 1000 times at 1 A g^{-1}. The storage mechanism of the aqueous zinc–iodine (Zn//I$_2$) battery with high energy density depends on the dissolution–deposition reaction. However, the monomeric I$_2$ cathode tends to form the highly soluble I$_3$$^-$ ions dissolving in the electrolyte, and the soluble ions will penetrate the separator and react on the surface of the Zn anode (I$_3$$^-$ + Zn → Zn^{2+} + I$^-$), leading to problems such as self-discharge and low CE.[128–131] Isolating the direct contact between Zn anode and the I$_3$$^-$ ions is one of the most promising strategies for enhancing the stability of the Zn//I$_2$ battery. Therefore, the Sn protective layer constructed on the surface of the Zn anode *in situ* could isolate the direct contact between the Zn anode and the dissolved I$_3$$^-$ ions. Consequently, the electrochemical performance of the Zn//I$_2$ battery would be greatly improved.[128,131]

(iv) Carbon material coating. Carbon materials have the advantages of high electrical conductivity, good chemical stability, and rich pore structure, which can effectively enhance the performance of ZIBs when compounded with the ZIBs cathode active material or Zn anode.[132] Archer's group[133] developed a dendrite-free Zn anode with an epitaxial deposition mechanism by introducing a graphene (002) substrate (a low lattice mismatch of 7% between graphene and Zn metal). "Epitaxial deposition" could effectively drive Zn deposition with a locked crystal orientation relationship, fundamentally changing the irregular and non-planar electrodeposition of

Zn^{2+} ions at the liquid–solid interface. During the epitaxial deposition process, Zn was nucleated along the graphene (002) crystal plane orientation, forming an epitaxial layer with the same crystal orientation as the graphene substrate (heterogeneous epitaxial process). When the surface of the graphene substrate was completely covered by Zn deposition, a homogeneous epitaxial process would occur, and finally, a platelet stacking structure Zn deposition would be obtained (Fig. 12c). Electrochemical studies revealed that the epitaxial Zn anode's reversibility was greatly enhanced, with a CE of more than 99% even after thousands of cycles. Additionally, Li's group[134] assembled graphene (GN) and cellulose nano-whiskers (CNW) through CH–π interactions to construct a bifunctional cellulose nano-whisker-graphene (CNG) membrane. The CNG membrane had strong ductility and puncture resistance and could adapt to the volume change during plating/stripping. Moreover, through the attraction of CNW to water molecules and the repulsion of GN to water molecules, the CNG film could be used as a desolvation layer to promote the desolvation process of [Zn(H$_2$O)$_6$]$^{2+}$. Further, the CNG film with low electronic conductivity and high ionic conductivity had a negatively charged surface, shielding anions while promoting the diffusion of Zn^{2+} ions through the CNG layer (Fig. 12d) and achieving (002) crystal-oriented Zn deposition. Under this synergy, the CNG@Zn symmetric cell achieved an ultra-long lifetime of 5500 h at 0.25 mA cm^{-2}/0.5 mA h cm^{-2}, which was more than 27 times that of the bare Zn anode. The CNG@Zn//MnO$_2$ full cell has a discharge capacity of up to 307 mA h g^{-1} and a capacity retention rate of 87.8% even after 5000 cycles at 5C.

4.2.2 Organic coating. Organic coatings have the benefits of excellent adhesion, hydrophilicity, high ionic conductivity, and mechanical strength, which have immense application prospects in Zn anode protection. Guo's group[135] used a spin-coating strategy to uniformly coat a highly viscoelastic insulating polyvinyl butyral (PVB) film on the Zn surface as an artificial SEI layer. The PVB coating was rich in oxygen-containing functional groups that effectively prevented water molecules and anions from passing through the PVB layer, while the high electrical resistance and high ionic conductivity of the PVB coating facilitated driving the diffusion of Zn^{2+} ions. The polyvinyl alcohol group also provided active sites or solventized groups for ion transfer, which increased the Zn^{2+} ion migration number (t_{Zn}^{2+} = 0.68 vs. 0.34) and effectively inhibited side reactions and dendrite growth (Fig. 13a). The cycle life of the PVB@Zn symmetric cell exceeded 2200 h at a current density of 0.5 mA cm^{-2}. The PVB@Zn//MnO$_2$ full cell had a capacity retention of 86.6% after 1500 cycles at 5C (the corresponding Zn//MnO$_2$ cell capacity retention was only 31.8%). Since poly-acrylonitrile (PAN) had great chemical stability and thermal stability, Van Ree's group[136] produced a hydrophilic porous artificial polyacrylonitrile dendrite suppression film (PANZ@Zn) by dropping a PAN solution containing Zn(TfO)$_2$ onto the surface of Zn foil. The polymer network and Zn^{2+} ion transport channels in the PNAZ film could well regulate the ion transport pathways during the electrochemical reaction, enabling uniform Zn deposition on the Zn substrate surface, thus effectively avoiding the

formation of dendrites (Fig. 13b). The PANZ@Zn anode exhibited excellent electrochemical stripping and deposition performance. At 1 mA cm^{-2}/1 mA h cm^{-2}, the PANZ@Zn symmetric cell had a long cycle of more than 1140 h, and the rate performance and long-term cycle performance of the PANZ@Zn//MnVO full cell were also greatly improved. Lee's group[137] designed an ionic liquid gel protective coating layer (ILG@Zn) consisting of hydrophobic IL solvents ((BMPTFSI), Zn(TFSI)$_2$) and mercapto-ene polymer compatible skeleton (TMPMP, TMPTA) up to 500 nm thick. The ILG coating prevented water molecules from directly contacting the Zn anode while allowing Zn^{2+} ions to diffuse through the coating layer (Fig. 13c). Among other things, BMP$^+$ ions had a shielding effect and facilitated uniform Zn deposition. The mercapto-ene polymer compatible skeleton allowed the IL gel film to adhere to the Zn foil surface and maintain structural integrity during the Zn plating and stripping process. The ILG@Zn symmetric cell was tested to exhibit stable and sustainable cycling performance over 1000 h, and the capacity retention of the ILG@Zn//MnO$_2$ cell was 95.7% after 600 cycles. Qian's group[138] improved the wettability of the electrode–electrolyte interface by coating the Zn anode surface with a conductive polymer (polypyrrole, PPy) to promote the diffusion and uniform nucleation of Zn^{2+} ions. The presence of an aromatic ring caused the ppy coating to be negatively charged, which facilitated the adsorption of Zn^{2+} ions in the ppy coating and greatly reduced the reaction impedance ($R_{CT,Zn@PPy}$ = 25 Ω vs. $R_{CT,Zn}$ = 70 Ω). In addition, the strong interaction of Zn^{2+} ions with polar groups
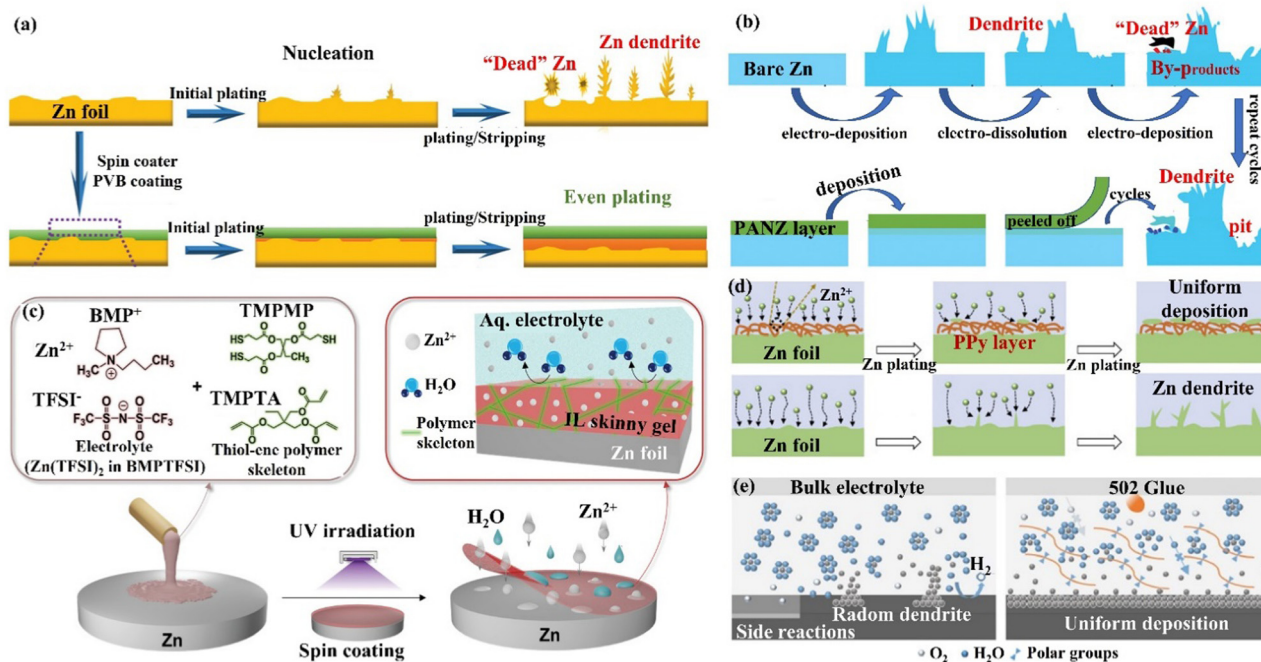

Fig. 13 A schematic diagram of (a) the morphological evolution of bare Zn and the PVB@Zn anode during repeated cycles. Reproduced with permission from ref. 135. Copyright 2020, Wiley-VCH. (b) Zn deposition behavior on bare Zn and the PANZ@Zn anode. Reproduced with permission from ref. 136. Copyright 2021, Wiley-VCH. (c) The process of preparation of IL thin gels, and the chemical composition and protection mechanism of IL coating. Reproduced with permission from ref. 137. Copyright 2021, Wiley-VCH. (d) Zn deposition process on the Zn foil and the PPy@Zn anode. Reproduced with permission from ref. 138. Copyright 2020, Elsevier Inc. (e) The behaviors of Zn deposition and side reactions on Zn foil and 502-glue@Zn surfaces, and the modification mechanism of 502 coatings. Reproduced with permission from ref. 139. Copyright 2020, Elsevier Inc.

in ppy further reduced the local Zn^{2+} ion concentration and promoted the horizontal growth of Zn (Fig. 13d). The PPy@Zn symmetric cell could achieve more than 540 cycles at 2 mA cm^{-2}, and the PPy@Zn//δ-MnO$_2$ full cell had a capacity of 205 mA h g^{-1} after 200 cycles with a capacity retention rate of 92%. Shen's group[139] evenly coated a cyanoacrylate adhesive (502-glue) with strong adhesion as a protective layer by spin coating on Zn foil surface. There was a rich polar bonding network in this coating skeleton, which could effectively trap solventized water molecules and prevent the electrode from direct contact with active water molecules and oxygen, greatly inhibiting the side reactions. The 502-glue coating also acted as a solid diffusion barrier, which regulated the nucleation overpotential by increasing the ion diffusion barrier, resulting in a uniform Zn^{2+} ion flux at the interface and inducing uniform Zn deposition under the coating (Fig. 13e). The 502-glue@Zn anode had a higher corrosion potential, greater resistivity, and good Zn^{2+} ion conductivity. At 0.5 mA cm^{-2}/0.25 mA h cm^{-2}, the 502-glue@Zn symmetric cell was cycled stably for 800 h, and even when the current density was increased to 2 mA cm^{-2} and 4 mA cm^{-2}, the 502-glue@Zn anode still had excellent stability. The 502-glue@Zn//V$_2$O$_5$ full cell had a higher initial capacity (160.8 mA h g^{-1}) and good rate performance, with a capacity retention of 59.3% after 550 cycles. Covalent organic frameworks (COFs), also known as "organic zeolites", are crystalline materials with a 2D topology formed by the covalent bonding of light atoms (hydrogen, boron, carbon, nitrogen, etc.).[140–144] Guo's group[141] developed an ultrathin fluorinated 2D porous COF film (FCOF) as a protective layer for Zn anodes. The strong interaction between F and Zn atoms greatly facilitated the Zn deposition along the (002) plane. Moreover, the 2D stacking and covalent bonding endowed the FCOF film with a high elastic modulus (> 30 GPa), which alleviated volume expansion during cycling. With this 2D COF design, the FCOF@Zn anode has excellent reversibility and cycle life. Even at ultra-high current densities of 40 mA cm^{-2}, the FCOF@Zn symmetric cell can be stable for over 750 h and the FCOF@Zn//MnO$_2$ full cell could be stably cycled for more than 250 cycles. Lan's group[144] explored a series of metal–covalent organic frameworks to inhibit dendrite growth and the HER. The hydrogen production of the battery was only 0.002 mmol h^{-1} cm^{-2}, which is 2 orders of magnitude lower than that of the bare zinc battery. Notably, the symmetric cell is stable for 3000 cycles, even at 20 mA cm^{-2} with an overpotential of only 79.1 mV. When matching with the MnO$_2$ cathode, the full cell provides a cycling stability of up to 6000 cycles at 2 A g^{-1} (discharge capacity of 217.2 mA h g^{-1}).

4.2.3 Inorganic/organic hybrid coating. To address the problems of side reactions and uncontrolled Zn deposition on the Zn anode surface, Qie's group[145] introduced an anti-corrosive elastic constraint (AEC) layer of Zn anode based on TiO$_2$ nanoparticles and polyvinylidene fluoride (PVDF), which could significantly improve the uniform deposition and thermodynamic stability of the Zn anode. The AEC@Zn symmetric cell achieved a long stable cycle of 2000 h, with a lifetime of more than 250 h even at a high current density (8.85 mA cm^{-2}, DOD$_{Zn}$ = 60%). Poor wettability will lead to the growth of Zn dendrites, thus Pan's group[146] reconstructed the electrode/electrolyte interface by

introducing a nano-metal–organic framework (PVDF + UiO-66 MOF) protective layer on the surface of the Zn anode to resolve this issue. The hydrophilic MOFs material could improve the wettability of the Zn foil electrode surface, and the MOF nanoparticles were connected to form a nanoscale electrolyte reservoir layer, enabling fast Zn^{2+} ion transport and uniform Zn deposition (Fig. 14a). The UiO-66 MOF@Zn symmetric cell could be cycled more than 500 times at 3 mA cm^{-2} and maintained stable electrochemical cycling even at 7.5 mA cm^{-2}. Xu's group[147] also introduced a ZIF-8 porous coating, where the porous channels in the ZIF-8 coating can homogenize the Zn^{2+} ion flux and effectively inhibit the formation of Zn dendrites (Fig. 14b). Under high rate conditions, the migration/replenishment rate of cations in the electrolyte to the reaction interface and the uniformity of ion distribution at the interface are the key factors affecting the morphology of metal deposition. Xin's group[148] constructed a tunneling-rich and corona-polarized ferroelectric polymer-inorganic composite film coating (Poled BTO-coated Zn), which could achieve uniform distribution and self-accelerated migration of Zn^{2+} ions on the surface of Zn foil. The nano-porous structure of the ferroelectric coating provided a large number of uniform and ordered tunnels for ion transport, which promoted the uniformity of Zn^{2+} ion distribution and transport (nano-porous tunneling effect) (Fig. 14c). Moreover, the pre-polarized ferroelectric coating had a ferroelectric effect, and Zn^{2+} ions were driven by the electric field within the ferroelectric layer and showed a self-acceleration phenomenon. With the directional polarization of the ferroelectric layer, the poled BTO@Zn electrode had fewer surface by-products after the charge/discharge processes. At 1 mA cm^{-2}, the poled BTO@Zn symmetric cell could cycle steadily for more than 4000 h. Even at ultra-high current densities of 10 mA cm^{-2}, 20 mA cm^{-2}, and 40 mA cm^{-2}, they were stable for more than 1200 h, 600 h, and 225 h, respectively. The poled BTO@Zn//MnO$_2$ full cell exhibited high cycle stability for over 1000 cycles.

4.3 Electrolyte optimization

The stability of the Zn anode can be successfully improved by optimizing the electrolyte, except for the electrode material protection approaches. The presence of electrolytes provides an effective path for the transmission of Zn^{2+} ions in the battery system, which is one of the important aspects that affect the energy storage of the battery system. Compared with organic electrolytes, the cost of aqueous electrolytes is lower, and safety and ionic conductivity are significantly improved. However, aqueous electrolytes also face some challenges such as narrow electrochemically stable potential window (ESPW) (~ 1.23 V), Zn^{2+} ions forming a solvated structure $Zn(H_2O)_6^{2+}$ with water molecules, and the decomposition of water molecules leads to side reactions such as HER and corrosion.[149] Therefore, when optimizing the electrolyte, the following points must be met: (i) improve the transfer of Zn^{2+} ions and induce uniform Zn deposition. (ii) Diminish the content of active water in the electrolyte to inhibit side reactions. (iii) Widen the electrochemical stable potential window (ESPW) so that the electrode material can work at high voltage. (iv) Change the structure of
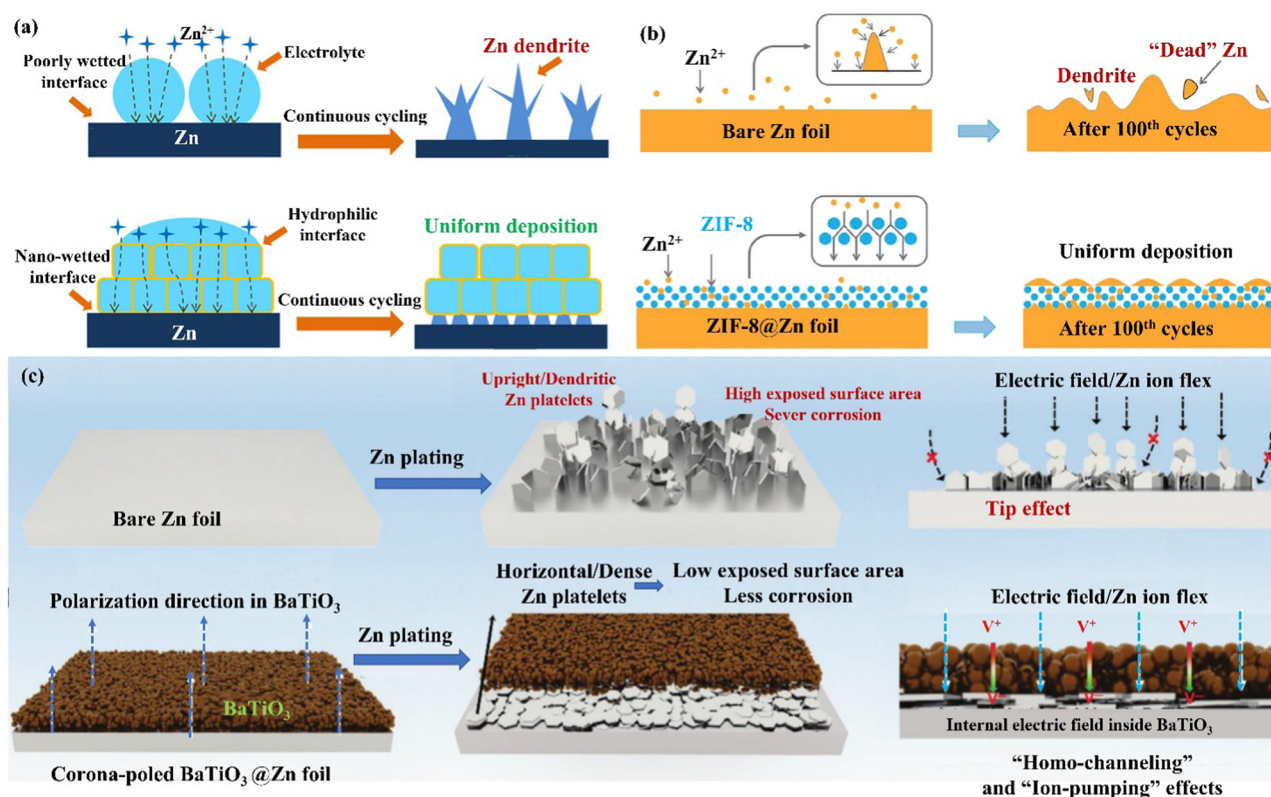
Fig. 14 (a) A schematic diagram of the Zn deposition mechanism on bare Zn and MOF−PVDF@Zn. Reproduced with permission from ref. 146. Copyright 2019, American Chemical Society. (b) Morphology evolutions for Zn foil and the ZIF-8@Zn electrode during repeated Zn plating/stripping processes. Reproduced with permission from ref. 147. Copyright 2020, Springer Nature. (c) A schematic diagram of Zn deposition morphology, electric field, and ion flux distribution on bare Zn and poled BTO-coated Zn. Reproduced with permission from ref. 148. Copyright 2021, Wiley-VCH.

the Zn solvate and reduce the impact of the desolvation process. Some of the additives are able to adsorb on the surface of the Zn electrode or react with the Zn electrode to form a compositionally controlled and structurally stable SEI layer *in situ*. This SEI layer significantly enhances the stability of the electrode–electrolyte interface. This section optimizes the types of Zn salts and electrolyte additives to improve battery performance.

4.3.1 Zn salt electrolyte. A series of zinc salts have recently been used in AZIBs, such as $ZnSO_4$,[150] $Zn(CH_3COO)_2$,[150] $Zn(ClO_4)_2$,[150–152] $ZnCl_2$,[153–155] $Zn(TFSI)_2$,[156,157] and other zinc salt electrolytes. Although they can be stably applied to AZIBs, they still face problems such as dendrite growth and side reactions, so it is necessary to further explore new zinc salt electrolytes with excellent performance.

$ZnSO_4$ with a regular tetrahedral structure has a strong polar S–O bond, and good stability.[150] However, during the charging and discharging process, serious side reactions still occur, producing insulation by-products such as ZHS and $Zn_4(OH)_6SO_4 \cdot nH_2O$. The insulation by-products covered the surface of the Zn electrode, leading to an increase in overpotential and hindering the migration of Zn^{2+} ions, and caused a decline in electrochemical performance and stability. The Zn symmetric cell using $ZnSO_4$ as the electrolyte could cycle steadily for 70 h while maintaining a CE of 99.1% at 0.5 mA cm^{-2}.

In contrast, the presence of larger $CF_3SO_3^-$ and TFSI$^-$ anions in $Zn(CH_3COO)_2$ and $Zn(TFSI)_2$ reduces the number of coordinated water molecules surrounding Zn^{2+} ions, decreases the degree of solvation with H_2O, and facilitates the migration of Zn^{2+} ions, which alleviated the side reaction to achieve higher reversibility.[150,157] However, the dendrite growth caused by an uneven electric field and ion distribution was not significantly improved, and the Zn symmetric cell with $Zn(CF_3SO_3)_2$ and $Zn(TFSI)_2$ electrolytes could be cycled stably for 220 h and 175 h, respectively.

Through the continuous development of high-performance zinc salt electrolytes, Sun's group[150] found that $Zn(ClO_4)_2$ electrolytes could significantly improve the electrochemical performance of AZIBs. During the charging and discharging process, ClO_4^- anions were reduced to form a thin protective layer containing Cl$^-$ ions, which inhibited the side reactions. The Zn symmetric cell containing the $Zn(ClO_4)_2$ electrolyte had excellent performance and achieved a high stability performance of more than 3500 h. However, at high temperatures, $Zn(ClO_4)_2$ electrolytes may pose safety risks, which limits its large-scale application in battery systems. Given the instability of the electrolyte in the cell, other methods are needed for optimization, such as adjusting the concentration of the electrolyte and introducing electrolyte additives.

4.3.2 Electrolyte additives. In response to different functional requirements (changing the solvation structure, forming

the SEI layer *in situ*, *etc.*), the electrochemical performance can be considerably enhanced by using particular electrolyte additives. For the selection of electrolyte additives, they need to meet the following requirements: (1) the number of Gutmann donors of electrolyte additives should be higher than H_2O, which can replace H_2O molecules and form a lower energy solvation structure with Zn^{2+} ions. (2) They can form a strong bond with H_2O molecules, reduce the activity of H_2O molecules and inhibit the reduction of H_2O molecules. (3) The oxidation–reduction reaction can occur preferentially, forming a dense SEI layer.

(i) The alteration of Zn^{2+} ions solvation structure. In the aqueous electrolyte, Zn^{2+} ions will coordinate with water molecules to form a $Zn[H_2O]_6^{2+}$ solvation structure, which additionally increases the energy required for the solvent removal process. In addition, the free water molecules removed during the desolvation process will be decomposed and reduced in contact with the Zn electrode, leading to side reactions such as corrosion, HER, passivation, and the generation of dendrites,

which diminish the utilization rate and cycle life of Zn. Mai's group[66] simultaneously controlled the solvation structure of Zn^{2+} ions and the uniform distribution of ions and electric field at the interface by introducing a trace amount of glucose molecules (low-cost and low concentration) into the $ZnSO_4$ electrolyte to construct a dendrite-free ZIBs (Fig. 15a). By replacing the water molecules in the solvation layer, glucose molecules effectively limited the occurrence of HER, Zn metal corrosion, and the generation of by-products. The organic molecular additives are promising for designing an advanced electrolyte. The polar groups can establish strong interactions with Zn^{2+} ions, water molecules and Zn surfaces, reconstruct the solvated structure of Zn^{2+} ions, build a hydrogen bond network, and preferentially adsorb on the Zn anode to form a zincophilic layer.[158] The glucose molecules adsorbed on the electrode surface also helped to shield the electric field at the tip, which prevented the dendrite growth. With this trace amount of glucose additives, the Zn symmetric cell could cycle

Fig. 15 The schematic diagram of (a) Zn deposition behaviors in $ZnSO_4$ and $ZnSO_4$–glucose electrolytes. Reproduced with permission from ref. 66. Copyright 2021, Wiley-VCH. (b) A schematic diagram of dendrite inhibition of $ZnSO_4/H_2O/EG$ hybrid electrolytes. Reproduced with permission from ref. 32. Copyright 2020, Elsevier Inc. (c) A schematic of Zn/electrolyte interphase behaviors during Zn plating in $ZnSO_4$ electrolyte and EDTA-functionalized $ZnSO_4$ electrolyte. Reproduced with permission from ref. 160. Copyright 2021, Wiley-VCH. (d) A diagram of the Zn^{2+} ions solvation structure, the corresponding nucleation and deposition behaviors in 2 M $ZnSO_4$ and DMSO-containing hybrid electrolytes. Reproduced with permission from ref. 36. Copyright 2021, Wiley-VCH.

steadily for more than 2000 h and 270 h at 1 mA cm^{-2}/ 1 mA h cm^{-2} and 5 mA cm^{-2}/5 mA h cm^{-2}, respectively. The Zn//MnO$_2$ full cell could be stable for more than 1000 cycles at 10 C, and the capacity can reach 265.6 mA h g^{-1} at 1C. Pan's group[32] regulated the coordination environment of Zn^{2+} ions by introducing alcohol additives, thereby inhibiting the growth of Zn dendrites (Fig. 15b). The research results showed that the polyol had a good coordination ability with Zn^{2+} ions, which was beneficial for controlling the growth of Zn dendrites.[159] For example, after adding ethylene glycol (EG) additives, part of the water molecules in the solvated [Zn(H$_2$O)$_6$]$^{2+}$ structure were replaced by EG molecules to form the [Zn(H$_2$O)$_m$(EG)$_n$]$^{2+}$ structure. This coordination structure reduced the desolvation energy of Zn^{2+} ions, and its larger size had a steric hindrance effect on the diffusion of Zn^{2+} ions. In the alcohol/water mixed electrolyte, the crystal grains of the deposition product were refined and the dendrite growth process was significantly inhibited. The Zn symmetric cell with 3 M ZnSO$_4$/H$_2$O/68 vol% EG electrolyte achieved a long cycle life (2668 h stable cycle at 0.5 mA cm^{-2}). Qiao's group[160] proposed a bifunctional electrolyte additive (ethylenediaminetetraacetic acid tetrasodium salt, Na$_4$EDTA) to improve the reversibility of the Zn anode. the EDTA anion preferentially adsorbed and covered the Zn anode surface, reducing the active sites of the HER (the hydrogen production of ZnSO$_4$ electrolyte containing Na$_4$EDTA additive was only 1/4 of the original electrolyte). The EDTA-adsorbed layer formed Zn^{2+} ion diffusion channels at the interface and the polar functional groups facilitated the desolvation process of Zn(H$_2$O)$_6^{2+}$, which allowed uniform Zn deposition (Fig. 15c). With this bifunctional electrolyte additive, the Zn symmetric cell achieved a CE of 99.5% after 2500 stable cycles at 5 mA cm^{-2}/2 mA h cm^{-2}, and the Zn//VO$_2$ full cell showed almost no capacity decay within 2000 cycles at 4 A g^{-1}. Wu's group[36] changed the solvation structure of Zn^{2+} ions and reconstructed the hydrogen bond (S=O···HO) by adding dimethyl sulfoxide (DMSO) additive to the ZnSO$_4$ electrolyte, significantly improving the battery performance and low-temperature applications. Compared with H$_2$O, the binding energy between DMSO and Zn^{2+} ions was greater than the Zn^{2+} ion's coordination to form a solvated structure ([Zn(H$_2$O)$_m$-(DMSO)$_n$]$^{2+}$), which increased the nucleation overpotential and corrosion potential of Zn^{2+} ions, improved the deposition kinetics of Zn^{2+} ions and inhibited the corrosion of Zn metal.[155] In addition, DMSO induced the deposition of Zn^{2+} ions on the (002) crystal plane, forming a hexagonal structure without dendrites (Fig. 15d). With the DMSO additive, the Zn symmetric cell was stable when cycled for more than 2100 h and 1200 h at 20 °C and −20 °C, respectively. The Zn//MnO$_2$ full cell could work stably for more than 3000 cycles and 300 cycles at 20 °C and −20 °C, respectively, and could maintain a reversible capacity of 140 mA h g^{-1} even at 10C (20 °C). With additives such as carbonyl-containing organic solvents (N-methyl-2-pyrrolidone, NMP),[161] polyhydroxy organics (maltose),[162] and phosphorus-functional group-containing molecules (TCEP-HCl),[163] and so on, the solvated structural rearrangement of Zn and the stabilization of the hydrogen bond network were

facilitated. This synergistic effect inhibited the formation of dendrites and side reactions caused by water splitting, which improved the Zn anode stability. These additives also provide new insights into the design of aqueous electrolytes.

(ii) The *in situ* formation of the SEI layer. The establishment of SEI can effectively block the contact between the electrolyte and the Zn anode surface to suppress side reactions. However, because of significant volume fluctuations during electrochemical cycling, these brittle SEI layers may be harmed and separated from the Zn surface. Moreover, the low ionic conductivity, Zn^{2+} ion migration number of artificial SEI layers and poor interfacial contact with Zn also lead to their limited enhancement for the stability of the Zn anode, and the formation of the *in situ* SEI layer can effectively solve these problems.[164–166] Cui's group[156,157] reported an acetamide (Ace) – Zn(TFSI)$_2$ eutectic electrolyte. TFSI$^-$ was able to coordinate with Zn^{2+} ions to form zinc complexes ([ZnTFSI$_m$(Ace)$_n$]$_{(2-m)}^+$), significantly reducing the decomposition energy of the TFSI$^-$ anion (Fig. 16a). This caused the reductive decomposition process of TFSI$^-$ to occur preferentially to the Zn deposition process (0.37 V *vs.* −0.76 V), favoring the *in situ* formation of mechanically rigid SEI layers (ZnF$_2$) (Fig. 16b). Through this improved zinc salt electrolyte, the Zn symmetric cell could maintain an average CE of 99.7% and achieve a stable cycle of more than 1000 h. The negatively charged MXene nanosheets could form a stable protective film, which might create a durable protective layer that would balance out the distribution of ions and reduce the path of Zn^{2+} ions during their diffusion.[167] Moreover, ample functional groups and the high electrical conductivity of the Mxene layer allowed for uniform Zn nucleation, the inhibition of dendritic growth, and the reduction of byproducts (Fig. 16c). Through the MXene nanosheet electrolyte additive, the Zn symmetric cell could be cycled stably for 1180 h, and the CE was as high as 99.7%. The Zn//V$_2$O$_5$ full cell exhibited high cycle stability with more than 300 cycles and maintained a reversible capacity of 192.9 mA h g^{-1} at 1 A g^{-1}. Wang's group[154] added 0.05 m SnCl$_2$ additive to the ZnCl$_2$ electrolyte to form a eutectic electrolyte, which effectively overcame the two challenges of disordered dendrite growth and poor low-temperature performance. The eutectic electrolyte could be reduced and decomposed to form a zincophilic Sn/zincophobic Zn$_5$(OH)$_8$Cl$_2$·H$_2$O double-layer interface phase *in situ* (Fig. 16d), and realize a stable performance at low temperature. The zincophilic Sn layer could reduce the overpotential of Zn deposition and promote uniform Zn deposition, while the zincophobic Zn$_5$(OH)$_8$Cl$_2$·H$_2$O top layer inhibited the growth of Zn dendrites. In addition, because the solvated Zn^{2+} ions and Cl$^-$ ions disrupted the hydrogen bond network, the eutectic electrolyte had a high ionic conductivity of 0.8 mS cm^{-1} even at a temperature of −70 °C. Thanks to the design of this eutectic electrolyte, the Zn symmetric cell could be stably cycled for more than 500 h at 3 mA cm^{-2} with an overpotential of only 8 mV. Moreover, even at −50 °C, the Zn//VOPO$_4$ full cell maintained a capacity of over 95% and a CE of 99.9% after 200 cycles. Guo's group[165] added 0.025 M Zn(H$_2$PO$_4$)$_2$ to 1 M Zn(CF$_3$SO$_3$)$_2$ to form a dense and uniform Zn phosphate SEI layer (2H$_2$PO$_4^-$ + 4OH$^-$ + 3Zn^{2+} → Zn$_3$(PO$_4$)$_2$·4H$_2$O↓, ∼140 nm). This Zn phosphate SEI layer had
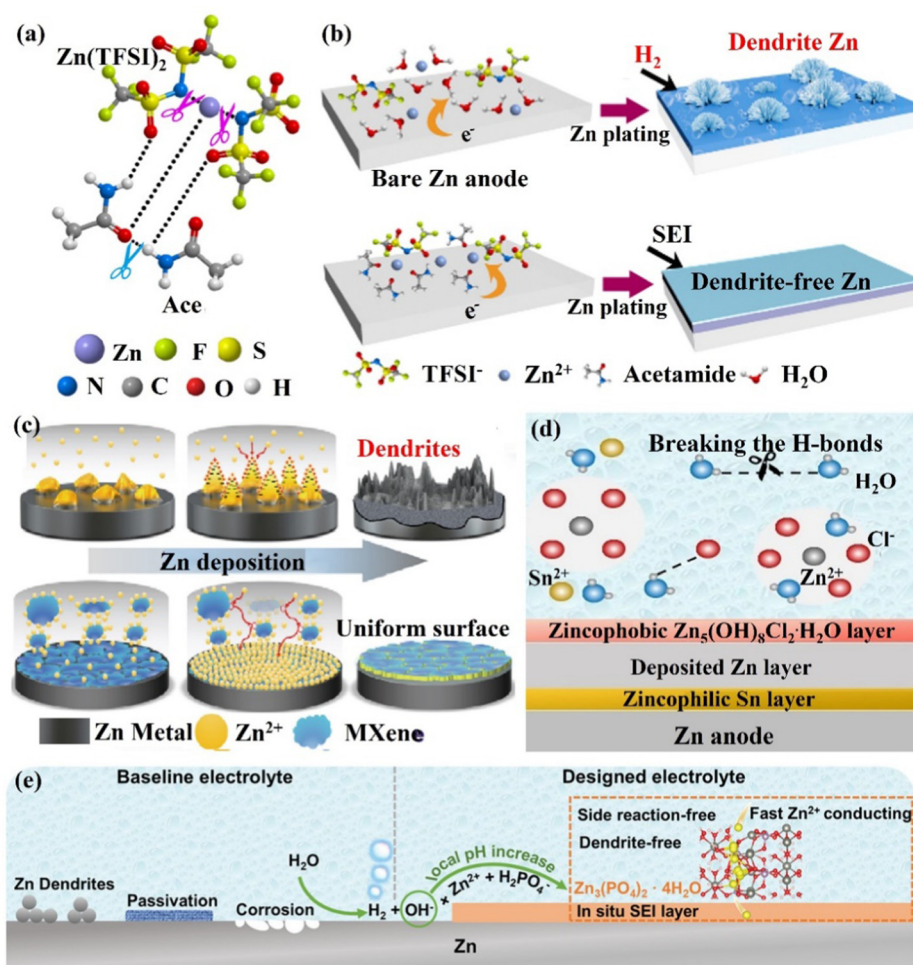
Fig. 16 Schematic diagrams of (a) Zn^{2+} ions, $TFSI^-$ ions, and Ace interacting to generate eutectic solutions, (b) Zn deposition in 1 M $Zn(TFSI)_2$ and the regulatory mechanism for achieving uniform Zn deposition with the SEI layer. Reproduced with permission from ref. 156. Copyright 2019, Springer Nature. (c) The regulation of Zn deposition by MXene additive. Reproduced with permission from ref. 167. Copyright 2021, Springer Nature. (d) The formation of SEI layers in the presence of $SnCl_2$ additive and its regulatory mechanism for Zn deposition. Reproduced with permission from ref. 154. Copyright 2021, Wiley-VCH. (e) The mechanism of zinc phosphate SEI layer generation and the control of Zn anode surface. Reproduced with permission from ref. 165. Copyright 2021, Wiley-VCH.

good interface stability, high ion mobility, and ion conductivity, ensuring a uniform and rapid diffusion process for Zn^{2+} ions, thereby achieving dendrite-free Zn deposition (Fig. 16e). This electrolyte design idea was also applicable to the $ZnSO_4$ system electrolyte. Through this *in situ* formation of SEI layer $Zn(H_2PO_4)_2$, the stable cycle performance of the $Zn//V_2O_5$ battery was significantly improved, and the capacity retention efficiency could still be as high as 94.4% after 500 cycles. Additives such as alkylammonium salts $(Me_3EtNOTF)$,[118] $ZnSe$,[168] and ZnF_2[169,170] could also help to form a composite interface *in situ* with high conductivity and waterproof performance, suppressing the HER, increasing the ECSW of the electrolyte, and achieving a highly reversible stable cycling performance.

4.3.3 Non-aqueous electrolytes. Although great progress has been made on aqueous electrolytes in AZIBs, problems such as narrow electrochemical windows, HER and corrosion on the Zn anode, and dissolution of the cathode active material

are still not completely eliminated. Therefore, the research on non-aqueous electrolytes has received extensive attention and development. Non-aqueous electrolytes mainly include all-solid-state polymer electrolytes (SPEs), hydrogel electrolytes (HEs) and other non-liquid electrolytes.[23,158,171–173] Compared with conventional aqueous electrolytes, non-aqueous electrolytes have many advantages, such as (1) having a wide electrochemical stability window, which is conducive to improving the actual energy density of the battery; (2) possessing high mechanical strength, alleviating the growth of dendrites and benefitting for wearable flexible devices; (3) reducing the direct contact between water molecules and the surface of the Zn anode to inhibit the HER and interfacial side reactions; (4) reducing the dissolution of active materials of the cathode and extending the life of the battery.

(i) All-solid-state polymer electrolyte. High mechanical strength is an inherent advantage of SPEs, which effectively solves the short-circuit problem caused by Zn dendrites in

aqueous electrolytes. Currently, SPEs based on polyethylene oxide (PEO), polyacrylonitrile (PAN), and polyvinyl chloride (PVC) have been widely studied due to their high mechanical strength, chemical stability, and flexibility. However, the low ionic conductivity (< 0.1 mS cm^{-1}) and poor interfacial contact of SPEs at room temperature limit their further development.[171,174,175] Research has shown that the crystallinity of SPEs could be significantly reduced and ionic conductivity greatly enhanced by (1) adding inorganic nanofillers (Al_2O_3, SiO_2, TiO_2, ZnO) to lower the phase transition temperature,[176–179] and (2) blending with low molecular weight polymers likes polyvinylidene fluoride (PVDF)[23] and branched aramid nanofibers.[180] Zhi's group[23,179] prepared a polyvinylidene fluoride-hexafluoropropylene/poly-ethylene oxide (PVDF-HFP/PEO) all-solid polymer electrolyte with high ionic conductivity (16.9 mS cm^{-1}), excellent flexibility and mechanical properties, which significantly inhibited both the HER and dendrite growth. Solid-state ZIBs based on PVDF-HFP/PEO exhibit excellent cycling stability and rate capability, enabling the operation in a wide temperature range from -20 °C to 70 °C. However, lower ionic conductivity and unstable interface still restrict the application of SPEs.

(ii) Hydrogel electrolytes (HEs). HEs exhibit excellent performance since they possess the properties of both liquid and solid materials. At present, several hydrogels have been successfully applied in functional AZIBs, such as polyvinyl alcohol (PVA),[181] polyacrylamide (PAM),[182–186] polyacrylic acid (PAA),[187] sodium polyacrylate (PANa),[158,188] zwitterionic sulfobetaine[189] and so on. These HEs exhibit high ionic conductivity from 10^{-3} to 10^{-1} S cm^{-1}, which is higher than that of SPEs. Compared with the aqueous electrolytes, HEs have many advantages, such as (1) strong hygroscopicity and water retention, which can effectively alleviate the loss of electrolyte; (2) uniformly distributed internal 3D network structure that facilitates the rapid transport of Zn^{2+} ions and dense Zn deposition; (3) reduced water content that significantly inhibits side reactions and dissolution of the active material.[190]

However, HEs are extremely easy to freeze at low temperatures, leading to the disappearance of the inherent advantage (flexibility) and the degradation of battery performance. Zhi's group[184] designed a glycol/polyacrylamide-based oil–water double-crosslinked hydrogel that exhibited a low freezing point, high ionic conductivity, high salt resistance, and strong mechanical stability (can pull stretch $\sim 900\%$). The ether groups introduced into the hydrogel matrix can form strong hydrogen bonds with free water molecules, effectively reducing the freezing point of the hydrogel and maintaining high ionic conductivity. Through this modification, the assembled flexible Zn//MnO$_2$ battery maintained a discharge capacity of 146 mA h g^{-1} at -20 °C, and the capacity retention rate was 72.54% of the initial capacity after 600 cycles. Nevertheless, HEs still face many challenges that need to be addressed. First, the inhomogeneous quasi-solid–electrode interface inevitably leads to large resistance, which requires improved preparation processes. Secondly, the mechanical properties of HEs are much inferior to SPEs, so a rational double cross-linking design is required to achieve HEs with both flexibility and mechanical stability.

Furthermore, it is still necessary to improve the stability of HEs over a wide temperature range.

(iii) Other non-liquid electrolytes. In addition to SPEs and HEs, other materials have been explored for non-liquid electrolytes. For example, quasi-solid electrolytes (PVC, PVDF, PVDF–HFP, polyethylene glycol diglycidyl ether (PEGDGE), tetraethylene glycol diacrylate (TEGDA)) consisting of liquid electrolyte (solvent) and polymer matrix and new inorganic high concentration colloidal electrolytes (HCCE). These have been extensively investigated to achieve excellent properties by tuning the compositions.[158,171,173,191]

5. Conclusions and outlook

The AZIBs are promising for application in the field of energy storage due to their inherent advantages such as abundant Zn metal reserves, environmental friendliness, low redox potential (-0.76 V $vs.$ SHE), and high theoretical capacity (820 mA h g^{-1} or 5855 mA h cm^{-3}). However, the poor reversibility of the Zn anode seriously hinders their practical large-scale applications. In this review, the intrinsic failure mechanisms of the Zn anode, influential factors on Zn deposition, and the state-of-the-art protection strategies for highly reversible Zn anode design are systematically summarized. Although significant progress has been achieved in the improvement of high-performance AZIBs, there are still some challenges for their future practical applications, and even some key issues that need attention have often been overlooked in the previous research. More attention should be paid to the zinc utilization, cost and battery energy density to meet the growing demand for the commercialization of zinc ion batteries. The future perspectives and development direction for the high-performance AZIBs are as follows:

5.1 Modulating the relationship between the depth of discharge (DOD)/CE and the reversibility of the Zn anode

Currently, the utilization rate of a Zn anode and the Coulombic efficiency (CE) of the electrochemical performance of batteries is still low for practical applications. The DOD represents the percentage of the Zn anode participating in the electrochemical reaction as compared to the total capacity of the entire Zn electrode. Battery life is affected by the DOD of the anode, which is an important parameter for measuring the utilization of electrode materials. This parameter is related to battery capacity decay and energy density. CE is also another important indicator for evaluating the cycle life and utilization of Zn anodes. At present, there is no unified standard for quantifying the CE and DOD of the Zn anode, and many studies have obtained high CE under the low DOD of the Zn anode, which lacks practical guiding significance for the development of AZIBs with high energy density. Therefore, it is significant to develop the Zn anodes with high CE under the high DOD for the development and application of AZIBs.

5.2 Selecting suitable types of zinc anode for ZIBs

Most zinc−ion batteries generally choose Zn flake as the anode and a low-loading mass of cathode for the related research.

The test conditions are relatively mild (high N/P ratio, low areal capacity, and so on), thus the actual energy density of the total battery system is very low, and it is far away from meeting the needs of practical applications. Although great progress has been made for the Zn flake anode in the lab, it has some shortcomings that are difficult for the Zn anode towards the commercialization of ZIBs as follows: (1) low utilization of Zn, which is not conducive to the construction of practical high-energy density electronic devices; (2) serious dendrite growth, which can easily pierce the separator and cause an internal short circuit; (3) repeated plating/stripping processes lead to the overall pulverization of the electrode, which results in the failure of the battery. Compared with Zn flake, Zn powder has more industrial application prospects as a Zn anode material. First, the loading quality of the Zn powder can be adjustable, which is conducive to the preparation of high-utilization Zn anodes and reduces the capacity ratio of negative/positive (N/P) electrodes to meet actual needs. Secondly, Zn powder has a more diversified processing technology, which also provides favorable conditions for constructing a dendrite-free Zn anode. However, the Zn powder anode increases the contact area between the electrode and the electrolyte, which inevitably leads to problems such as HER and side reactions. It is expected to facilitate the commercial application of Zn powder anodes by improving Zn powder binders, current collectors, and hybrid structures.

5.3 Application under extreme conditions

The ability to maintain high performance under extreme operating conditions (lean electrolyte, high current density, and wide temperature range, *etc.*) is very important for the commercialization of AZIBs. The electrolyte added to the ZIBs button cells assembled in the experimental stage is usually excessive, which not only seriously reduces the energy density of the battery but also can not directly reflect the problem of electrolyte consumption due to the occurrence of side reactions. In the case of ensuring the normal operation of the battery, the smaller the amount of electrolyte added, the higher the energy density of the AZIBs that can be achieved. Under the conditions of high current density, side reactions and other undesirable failures inside the battery will be more obvious, resulting in unstable battery performance and even short-circuit failure. In addition, aqueous electrolytes will freeze at low temperatures, resulting in decreased conductivity and reduced battery performance. These are the problems that need to be solved urgently in the process of commercial application of AZIBs. Seeking low-cost electrolytes or additives to maintain stable performance under extreme working conditions is also the main theme for the development of AZIBs.

5.4 Developing the flexible and stretchable wearable electronic devices

Based on the inherent safety performance of AZIBs, it is promising for flexible and stretchable electronics applications. Gel polymer electrolytes provide a great boost for the development of flexible aqueous electronic devices as a result of their great wettability, high flexibility and excellent mechanical strength. However, in order to ensure the performance and energy density of the battery, the thickness and weight of the gel electrolyte must also be fully considered. In addition, the self-healing substrates developed so far typically suffer from short lifespans due to the dehydration in air. More attention should be directed towards improving the resistance of water loss or developing new suitable packaging materials. Moreover, the effects of components such as flexible and stretchable separators, current collectors, and binders on the performance of AZIBs are still not studied enough, and are also crucial for the improvement of the performance of AZIBs.

5.5 Designing the battery automatic detection device

Real-time detection of battery electrochemical performance during charge and discharge can accurately reflect the stability of battery material. Therefore, it is necessary to design an *in situ* automatic battery detection device to precisely forecast the "battery failure time" which guarantees that the battery pack operates within a safe range. This rational device can implement battery parameter monitoring, battery state estimation, online fault diagnosis, and charging control for the battery, which can also respond in a timely manner when a failure occurs.

Conflicts of interest

There are no conflicts to declare.

Acknowledgements

References

1 S. Ma, M. Jiang, P. Tao, C. Song, J. Wu, J. Wang, T. Deng and W. Shang, *Prog. Nat. Sci.*, 2018, **28**, 653–666.
2 Y. Chen, T. Wang, H. Tian, D. Su, Q. Zhang and G. Wang, *Adv. Mater.*, 2021, **33**, 2003666.
3 M. Chen, Y. Zhang, G. Xing, S.-L. Chou and Y. Tang, *Energy Environ. Sci.*, 2021, **14**, 3323–3351.
4 X. Wu, J. Dong, M. Qiu, Y. Li, Y. Zhang, H. Zhang and J. Zhang, *Nanoscale Horiz.*, 2020, **5**, 359–365.
5 H. Li and A. Y. Elezzabi, *Nanoscale Horiz.*, 2020, **5**, 691–695.
6 E. Cha, M. Patel, S. Bhoyate, V. Prasad and W. Choi, *Nanoscale Horiz.*, 2020, **5**, 808–831.
7 G. Liu, H.-H. Wu, Q. Meng, T. Zhang, D. Sun, X. Jin, D. Guo, N. Wu, X. Liu and J.-K. Kim, *Nanoscale Horiz.*, 2020, **5**, 150–162.
8 C. Li, L. Wang, J. Zhang, D. Zhang, J. Du, Y. Yao and G. Hong, *Energy Storage Mater.*, 2022, **44**, 104–135.

9 W. Lu, C. Zhang, H. Zhang and X. Li, *ACS Energy Lett.*, 2021, **6**, 2765–2785.

10 T. Wang, C. Li, X. Xie, B. Lu, Z. He, S. Liang and J. Zhou, *ACS Nano*, 2020, **14**, 16321–16347.

11 F. Wan, X. Zhou, Y. Lu, Z. Niu and J. Chen, *ACS Energy Lett.*, 2020, **5**, 3569–3590.

12 Q. Zhang, J. Luan, Y. Tang, X. Ji and H. Wang, *Angew. Chem., Int. Ed.*, 2020, **59**, 13180–13191.

13 Y. Tian, Y. An, C. Wei, B. Xi, S. Xiong, J. Feng and Y. Qian, *Adv. Energy Mater.*, 2021, **11**, 2002529.

14 D. Selvakumaran, A. Pan, S. Liang and G. Cao, *J. Mater. Chem. A*, 2019, **7**, 18209–18236.

15 X. Li, Z. Chen, Y. Yang, S. Liang, B. Lu and J. Zhou, *Inorg. Chem. Front.*, 2022, **9**, 3986–3998.

16 Z. Liu, L. Qin, B. Lu, X. Wu, S. Liang and J. Zhou, *ChemSusChem*, 2022, **15**, e202200348.

17 Z. Liu, Y. Yang, S. Liang, B. Lu and J. Zhou, *Small Struct.*, 2021, **2**, 2100119.

18 D. Han, S. Wu, S. Zhang, Y. Deng, C. Cui, L. Zhang, Y. Long, H. Li, Y. Tao, Z. Weng, Q. H. Yang and F. Kang, *Small*, 2020, **16**, 2001736.

19 H. Tian, Z. Li, G. Feng, Z. Yang, D. Fox, M. Wang, H. Zhou, L. Zhai, A. Kushima, Y. Du, Z. Feng, X. Shan and Y. Yang, *Nat. Commun.*, 2021, **12**, 237.

20 Y. Zuo, K. Wang, P. Pei, M. Wei, X. Liu, Y. Xiao and P. Zhang, *Mater. Today Energy*, 2021, **20**, 100692.

21 B. Li, X. Zhang, T. Wang, Z. He, B. Lu, S. Liang and J. Zhou, *Nanomicro Lett.*, 2021, **14**, 6.

22 A. Naveed, A. Ali, T. Rasheed, X. Wang, P. Ye, X. Li, Y. Zhou, S. Mingru and Y. Liu, *J. Power Sources*, 2022, **525**, 231122.

23 L. Ma, S. Chen, N. Li, Z. Liu, Z. Tang, J. A. Zapien, S. Chen, J. Fan and C. Zhi, *Adv. Mater.*, 2020, **32**, 1908121.

24 M. Rosso, C. Brissot, A. Teyssot, M. Dollé, L. Sannier, J.-M. Tarascon, R. Bouchet and S. Lascaud, *Electrochim. Acta*, 2006, **51**, 5334–5340.

25 Y. Wang, Y. Wang, C. Chen, X. Chen, Q. Zhao, L. Yang, L. Yao, R. Qin, H. Wu, Z. Jiang and F. Pan, *Chem. Commun.*, 2021, **57**, 5326–5329.

26 Q. Yang, Q. Li, Z. Liu, D. Wang, Y. Guo, X. Li, Y. Tang, H. Li, B. Dong and C. Zhi, *Adv. Mater.*, 2020, **32**, 2001854.

27 J. Su, X. Yin, H. Zhao, H. Yang, D. Yang, L. He, M. Wang, S. Jin, K. Zhao, Y. Wang and Y. Wei, *Nano Lett.*, 2022, **22**, 1549–1556.

28 A. Pei, G. Zheng, F. Shi, Y. Li and Y. Cui, *Nano Lett.*, 2017, **17**, 1132–1139.

29 P. Biswal, S. Stalin, A. Kludze, S. Choudhury and L. A. Archer, *Nano Lett.*, 2019, **19**, 8191–8200.

30 S. Wang, Z. Wang, Y. Yin, T. Li, N. Chang, F. Fan, H. Zhang and X. Li, *Energy Environ. Sci.*, 2021, **14**, 4077–4084.

31 Y. Li, P. Wu, W. Zhong, C. Xie, Y. Xie, Q. Zhang, D. Sun, Y. Tang and H.-Y. Wang, *Energy Environ. Sci.*, 2021, **14**, 5563–5571.

32 R. Qin, Y. Wang, M. Zhang, Y. Wang, S. Ding, A. Song, H. Yi, L. Yang, Y. Song, Y. Cui, J. Liu, Z. Wang, S. Li, Q. Zhao and F. Pan, *Nano Energy*, 2021, **80**, 105478.

33 C. Han, W. Li, H. K. Liu, S. Dou and J. Wang, *Nano Energy*, 2020, **74**, 104880.

34 K. Wang, P. Pei, Z. Ma, H. Xu, P. Li and X. Wang, *J. Power Sources*, 2014, **271**, 65–75.

35 P. Chen, Y. Wu, Y. Zhang, T.-H. Wu, Y. Ma, C. Pelkowski, H. Yang, Y. Zhang, X. Hu and N. Liu, *J. Mater. Chem. A*, 2018, **6**, 21933–21940.

36 D. Feng, F. Cao, L. Hou, T. Li, Y. Jiao and P. Wu, *Small*, 2021, **17**, 2103195.

37 J. W. Diggle, A. R. Despic and J. O. M. Bockris, *J. Electrochem. Soc.*, 1969, **116**, 1503.

38 M. Fayette, H. J. Chang, I. A. Rodri Guez-Perez, X. Li and D. Reed, *ACS Appl. Mater. Interfaces*, 2020, **12**, 42763–42772.

39 H. E. M. Hussein, R. J. Maurer, H. Amari, J. J. P. Peters, L. Meng, R. Beanland, M. E. Newton and J. V. Macpherson, *ACS Nano*, 2018, **12**, 7388–7396.

40 J. Hao, X. Li, X. Zeng, D. Li, J. Mao and Z. Guo, *Energy Environ. Sci.*, 2020, **13**, 3917–3949.

41 F. R. McLarnon and E. J. Cairns, *J. Electrochem. Soc.*, 1991, **138**, 645–656.

42 F. Xie, H. Li, X. Wang, X. Zhi, D. Chao, K. Davey and S.-Z. Qiao, *Adv. Energy Mater.*, 2021, **11**, 2003419.

43 Q. Zhu, W. A. Saidi and J. C. Yang, *J. Phys. Chem. C*, 2017, **121**, 11251–11260.

44 H. Wang, D. Ning, L. Wang, H. Li, Q. Li, M. Ge, J. Zou, S. Chen, H. Shao, Y. Lai, Y. Zhang, G. Xing, W. K. Pang and Y. Tang, *Small*, 2022, **18**, 2107491.

45 H. Jia, Z. Wang, B. Tawiah, Y. Wang, C.-Y. Chan, B. Fei and F. Pan, *Nano Energy*, 2020, **70**, 104523.

46 Q. Li, H. Pan, W. Li, Y. Wang, J. Wang, J. Zheng, X. Yu, H. Li and L. Chen, *ACS Energy Lett.*, 2018, **3**, 2259–2266.

47 C. Li, X. Xie, S. Liang and J. Zhou, *Energy Environ. Mater.*, 2020, **3**, 146–159.

48 Y. Yin, S. Wang, Q. Zhang, Y. Song, N. Chang, Y. Pan, H. Zhang and X. Li, *Adv. Mater.*, 2020, **32**, 1906803.

49 Q. Yang, G. Liang, Y. Guo, Z. Liu, B. Yan, D. Wang, Z. Huang, X. Li, J. Fan and C. Zhi, *Adv. Mater.*, 2019, **31**, 1903778.

50 Z. Zhao, J. Zhao, Z. Hu, J. Li, J. Li, Y. Zhang, C. Wang and G. Cui, *Energy Environ. Sci.*, 2019, **12**, 1938–1949.

51 L. Qian, W. Yao, R. Yao, Y. Sui, H. Zhu, F. Wang, J. Zhao, C. Zhi and C. Yang, *Adv. Funct. Mater.*, 2021, **31**, 2105736.

52 Q. Li, A. Chen, D. Wang, Y. Zhao, X. Wang, X. Jin, B. Xiong and C. Zhi, *Nat. Commun.*, 2022, **13**, 3699.

53 P. Zengxia, *Nano Res. Energy*, 2022, **1**, e9120023.

54 Q. Li, A. Chen, D. Wang, Z. Pei and C. Zhi, *Joule*, 2022, **6**, 273–279.

55 W. Du, E. H. Ang, Y. Yang, Y. Zhang, M. Ye and C. C. Li, *Energy Environ. Sci.*, 2020, **13**, 3330–3360.

56 C. Cao, F. Liang, W. Zhang, H. Liu, H. Liu, H. Zhang, J. Mao, Y. Zhang, Y. Feng, X. Yao, M. Ge and Y. Tang, *Small*, 2021, **17**, 2102233.

57 J. Zhao, Z. Cong, J. Hu, H. Lu, L. Wang, H. Wang, O. I. Malyi, X. Pu, Y. Zhang, H. Shao, Y. Tang and Z. L. Wang, *Nano Energy*, 2022, **93**, 106893.

58 M. Zhu, H. Wang, W. Lin, D. Chan, H. Li, K. Wang, Y. Tang, T. Hao, S. Chen, O. I. Malyi, Y. Tang and Y. Zhang, *Small Struct.*, 2022, **3**, 2200016.

59 Y. Liu, X. Lu, F. Lai, T. Liu, P. R. Shearing, I. P. Parkin, G. He and D. J. L. Brett, *Joule*, 2021, **5**, 2845–2903.

60 A. Konarov, N. Voronina, J. H. Jo, Z. Bakenov, Y.-K. Sun and S.-T. Myung, *ACS Energy Lett.*, 2018, **3**, 2620–2640.

61 Z. Zhou, Y. Zhang, P. Chen, Y. Wu, H. Yang, H. Ding, Y. Zhang, Z. Wang, X. Du and N. Liu, *Chem. Eng. Sci.*, 2019, **194**, 142–147.

62 B. E. Hawkins, D. E. Turney, R. J. Messinger, A. M. Kiss, G. G. Yadav, S. Banerjee and T. N. Lambert, *Adv. Energy Mater.*, 2022, **12**, 2103294.

63 L. Hu, P. Xiao, L. Xue, H. Li and T. Zhai, *Energy Chem.*, 2021, **3**, 100052.

64 Q. Yang, L. Li, T. Hussain, D. Wang, L. Hui, Y. Guo, G. Liang, X. Li, Z. Chen, Z. Huang, Y. Li, Y. Xue, Z. Zuo, J. Qiu, Y. Li and C. Zhi, *Angew. Chem., Int. Ed.*, 2022, **61**, e202112304.

65 M. Zhou, S. Guo, G. Fang, H. Sun, X. Cao, J. Zhou, A. Pan and S. Liang, *J. Energy Chem.*, 2021, **55**, 549–556.

66 P. Sun, L. Ma, W. Zhou, M. Qiu, Z. Wang, D. Chao and W. Mai, *Angew. Chem., Int. Ed.*, 2021, **60**, 18247–18255.

67 X.-B. Cheng, R. Zhang, C.-Z. Zhao and Q. Zhang, *Chem. Rev.*, 2017, **117**, 10403–10473.

68 W. Xu, J. Wang, F. Ding, X. Chen, E. Nasybulin, Y. Zhang and J.-G. Zhang, *Energy Environ. Sci.*, 2014, **7**, 513–537.

69 Y. Okajima, Y. Shibuta and T. Suzuki, *Comput. Mater. Sci.*, 2010, **50**, 118–124.

70 X. Zhang, A. Wang, X. Liu and J. Luo, *Acc. Chem. Res.*, 2019, **52**, 3223–3232.

71 C. Brissot, M. Rosso, J. N. Chazalviel, P. Baudry and S. Lascaud, *Electrochim. Acta*, 1998, **43**, 1569–1574.

72 Z. Hou, Y. Gao, R. Zhou and B. Zhang, *Adv. Funct. Mater.*, 2022, **32**, 2107584.

73 M. K. Aslam, Y. Niu, T. Hussain, H. Tabassum, W. Tang, M. Xu and R. Ahuja, *Nano Energy*, 2021, **86**, 106142.

74 X. Gao, Y.-N. Zhou, D. Han, J. Zhou, D. Zhou, W. Tang and J. B. Goodenough, *Joule*, 2020, **4**, 1864–1879.

75 H. Glatz, E. Tervoort and D. Kundu, *ACS Appl. Mater. Interfaces*, 2020, **12**, 3522–3530.

76 J. Zhi, S. Li, M. Han and P. Chen, *Sci. Adv.*, 2022, **6**, eabb1342.

77 Y. Han, Y. Jie, F. Huang, Y. Chen, Z. Lei, G. Zhang, X. Ren, L. Qin, R. Cao and S. Jiao, *Adv. Funct. Mater.*, 2019, **29**, 1904629.

78 K. Yan, J. Wang, S. Zhao, D. Zhou, B. Sun, Y. Cui and G. Wang, *Angew. Chem., Int. Ed.*, 2019, **58**, 11364–11368.

79 A. C. Thenuwara, P. P. Shetty and M. T. McDowell, *Nano Lett.*, 2019, **19**, 8664–8672.

80 H. Li, H. Wang, Z. Xu, K. Wang, M. Ge, L. Gan, Y. Zhang, Y. Tang and S. Chen, *Small*, 2021, **17**, 2103679.

81 S. Zhang, Z. Zhang, Y. Si, B. Li, F. Deng, L. Yang, X. Liu, W. Dai and S. Luo, *ACS Nano*, 2021, **15**, 15238–15248.

82 M. Ge, C. Cao, F. Liang, R. Liu, Y. Zhang, W. Zhang, T. Zhu, B. Yi, Y. Tang and Y. Lai, *Nanoscale Horiz.*, 2020, **5**, 65–73.

83 Q. Cao, H. Gao, Y. Gao, J. Yang, C. Li, J. Pu, J. Du, J. Yang, D. Cai, Z. Pan, C. Guan and W. Huang, *Adv. Funct. Mater.*, 2021, **31**, 2103922.

84 W. Guo, Z. Cong, Z. Guo, C. Chang, X. Liang, Y. Liu, W. Hu and X. Pu, *Energy Storage Mater.*, 2020, **30**, 104–112.

85 Y. Zhou, X. Wang, X. Shen, Y. Shi, C. Zhu, S. Zeng, H. Xu, P. Cao, Y. Wang, J. Di and Q. Li, *J. Mater. Chem. A*, 2020, **8**, 11719–11727.

86 J. Hao, B. Li, X. Li, X. Zeng, S. Zhang, F. Yang, S. Liu, D. Li, C. Wu and Z. Guo, *Adv. Mater.*, 2020, **32**, 2003021.

87 J. Hao, X. Li, S. Zhang, F. Yang, X. Zeng, S. Zhang, G. Bo, C. Wang and Z. Guo, *Adv. Funct. Mater.*, 2020, **30**, 2001263.

88 L. Kang, M. Cui, F. Jiang, Y. Gao, H. Luo, J. Liu, W. Liang and C. Zhi, *Adv. Energy Mater.*, 2018, **8**, 1801090.

89 H. Li, C. Guo, T. Zhang, P. Xue, R. Zhao, W. Zhou, W. Li, A. Elzatahry, D. Zhao and D. Chao, *Nano Lett.*, 2022, **22**, 4223–4231.

90 P. Liu, X. Ling, C. Zhong, Y. Deng, X. Han and W. Hu, *Front. Chem.*, 2019, **7**, 656.

91 J. Zhao, H. Lu, Y. Zhang, S. Yu, O. I. Malyi, X. Zhao, L. Wang, H. Wang, J. Peng, X. Li, Y. Zhang, S. Chen, H. Pan, G. Xing, C. Lu, Y. Tang and X. Chen, *Sci. Adv.*, 2021, **7**, eabd6978.

92 J. F. Parker, C. N. Chervin, I. R. Pala, M. Machler and D. R. Rolison, *Science*, 2017, **356**, 415–418.

93 Z. Kang, C. Wu, L. Dong, W. Liu, J. Mou, J. Zhang, Z. Chang, B. Jiang, G. Wang, F. Kang and C. Xu, *ACS Sustainable Chem. Eng.*, 2019, **7**, 3364–3371.

94 Y. An, Y. Tian, S. Xiong, J. Feng and Y. Qian, *ACS Nano*, 2021, **15**, 11828–11842.

95 M. Ge, Y. Tang, O. I. Malyi, Y. Zhang, Z. Zhu, Z. Lv, X. Ge, H. Xia, J. Huang, Y. Lai and X. Chen, *Small*, 2020, **16**, 2002094.

96 Y. Tang, Y. Zhang, O. I. Malyi, N. Bucher, H. Xia, S. Xi, Z. Zhu, Z. Lv, W. Li, J. Wei, M. Srinivasan, A. Borgna, M. Antonietti, Y. Du and X. Chen, *Adv. Mater.*, 2018, **30**, 1802200.

97 Y. An, Y. Tian, L. Ci, S. Xiong, J. Feng and Y. Qian, *ACS Nano*, 2018, **12**, 12932–12940.

98 Y. Zeng, X. Zhang, R. Qin, X. Liu, P. Fang, D. Zheng, Y. Tong and X. Lu, *Adv. Mater.*, 2019, **31**, 1903675.

99 H. Gan, J. Wu, R. Li, B. Huang and H. Liu, *Energy Storage Mater.*, 2022, **47**, 602–610.

100 Y. Hao, J. Zhou, G. Wei, A. liu, Y. Zhang, Y. Mei, B. Lu, M. Luo and M. Xie, *ACS Appl. Energy Mater.*, 2021, **4**, 6364–6373.

101 J. Zhou, M. Xie, F. Wu, Y. Mei, Y. Hao, R. Huang, G. Wei, A. Liu, L. Li and R. Chen, *Adv. Mater.*, 2021, **33**, 2101649.

102 P. Xue, C. Guo, L. Li, H. Li, D. Luo, L. Tan and Z. Chen, *Adv. Mater.*, 2022, **34**, 2110047.

103 Y. Tian, Y. An, C. Wei, B. Xi, S. Xiong, J. Feng and Y. Qian, *ACS Nano*, 2019, **13**, 11676–11685.

104 Y. Tian, Y. An, C. Liu, S. Xiong, J. Feng and Y. Qian, *Energy Storage Mater.*, 2021, **41**, 343–353.

105 Y. Zhang, Z. Cao, S. Liu, Z. Du, Y. Cui, J. Gu, Y. Shi, B. Li and S. Yang, *Adv. Energy Mater.*, 2022, **12**, 2103979.

106 D. Sha, C. Lu, W. He, J. Ding, H. Zhang, Z. Bao, X. Cao, J. Fan, Y. Dou, L. Pan and Z. Sun, *ACS Nano*, 2022, **16**, 2711–2720.

107 Y. Zhang, J. D. Howe, S. Ben-Yoseph, Y. Wu and N. Liu, *ACS Energy Lett.*, 2021, **6**, 404–412.

108 H. Chen, C. Dai, F. Xiao, Q. Yang, S. Cai, M. Xu, H. J. Fan and S.-J. Bao, *Adv. Mater.*, 2022, **34**, 2109092.

109 S. B. Wang, Q. Ran, R. Q. Yao, H. Shi, Z. Wen, M. Zhao, X. Y. Lang and Q. Jiang, *Nat. Commun.*, 2020, **11**, 1634.

110 J. Zheng, Z. Huang, Y. Zeng, W. Liu, B. Wei, Z. Qi, Z. Wang, C. Xia and H. Liang, *Nano Lett.*, 2022, **22**, 1017–1023.

111 H. Yan, S. Li, Y. Nan, S. Yang and B. Li, *Adv. Energy Mater.*, 2021, **11**, 2100186.

112 Q. Zhang, J. Luan, X. Huang, Q. Wang, D. Sun, Y. Tang, X. Ji and H. Wang, *Nat. Commun.*, 2020, **11**, 3961.

113 G. Liu, H. G. Yang, X. Wang, L. Cheng, H. Lu, L. Wang, G. Q. Lu and H.-M. Cheng, *J. Phys. Chem. C*, 2009, **113**, 21784–21788.

114 J. Y. Kim, G. Liu, G. Y. Shim, H. Kim and J. K. Lee, *Adv. Funct. Mater.*, 2020, **30**, 2004210.

115 P. Cao, X. Zhou, A. Wei, Q. Meng, H. Ye, W. Liu, J. Tang and J. Yang, *Adv. Funct. Mater.*, 2021, **31**, 2100398.

116 Y. Yang, C. Liu, Z. Lv, H. Yang, Y. Zhang, M. Ye, L. Chen, J. Zhao and C. C. Li, *Adv. Mater.*, 2021, **33**, 2007388.

117 J. Han, H. Euchner, M. Kuenzel, S. M. Hosseini, A. Groß, A. Varzi and S. Passerini, *ACS Energy Lett.*, 2021, **6**, 3063–3071.

118 L. Cao, D. Li, T. Pollard, T. Deng, B. Zhang, C. Yang, L. Chen, J. Vatamanu, E. Hu, M. J. Hourwitz, L. Ma, M. Ding, Q. Li, S. Hou, K. Gaskell, J. T. Fourkas, X.-Q. Yang, K. Xu, O. Borodin and C. Wang, *Nat. Nanotechnol.*, 2021, **16**, 902–910.

119 D. Wang, D. Lv, H. Peng, N. Wang, H. Liu, J. Yang and Y. Qian, *Nano Lett.*, 2022, **22**, 1750–1758.

120 G. Liang, J. Zhu, B. Yan, Q. Li, A. Chen, Z. Chen, X. Wang, B. Xiong, J. Fan, J. Xu and C. Zhi, *Energy Environ. Sci.*, 2022, **15**, 1086–1096.

121 W. Guo, Y. Zhang, X. Tong, X. Wang, L. Zhang, X. Xia and J. Tu, *Mater. Today Energy*, 2021, **20**, 100675.

122 S. Zhai, X. Shi, K. Jiang, X. Tan, W. Zhang, J. Zhang, H. Zhang and Z. Li, *Chem. Eng. J.*, 2022, **437**, 135246.

123 H. Yu, Y. Zeng, W. Li Nian, D. Luan, L. Yu and W. Lou Xiong, *Sci. Adv.*, 2022, **8**, eabm5766.

124 Y. Shi, Y. Chen, L. Shi, K. Wang, B. Wang, L. Li, Y. Ma, Y. Li, Z. Sun, W. Ali and S. Ding, *Small*, 2020, **16**, 2000730.

125 K. Ouyang, D. Ma, N. Zhao, Y. Wang, M. Yang, H. Mi, L. Sun, C. He and P. Zhang, *Adv. Funct. Mater.*, 2022, **32**, 2109749.

126 C. Liu, Z. Luo, W. Deng, W. Wei, L. Chen, A. Pan, J. Ma, C. Wang, L. Zhu, L. Xie, X.-Y. Cao, J. Hu, G. Zou, H. Hou and X. Ji, *ACS Energy Lett.*, 2021, **6**, 675–683.

127 H. Jia, Z. Wang, M. Dirican, S. Qiu, C. Y. Chan, S. Fu, B. Fei and X. Zhang, *J. Mater. Chem. A*, 2021, **9**, 5597–5605.

128 J. Ma, M. Liu, Y. He and J. Zhang, *Angew. Chem., Int. Ed.*, 2021, **60**, 12636–12647.

129 D. Lin, D. Rao, S. Chiovoloni, S. Wang, J. Q. Lu and Y. Li, *Nano Lett.*, 2021, **21**, 4129–4135.

130 W. Shang, Q. Li, F. Jiang, B. Huang, J. Song, S. Yun, X. Liu, H. Kimura, J. Liu and L. Kang, *Nanomicro Lett.*, 2022, **14**, 82.

131 T. Yadong, C. Song, H. Yulong, C. Qianwu, Z. Lili and Z. Jintao, *Nano Res. Energy*, 2022, DOI: 10.26599/NRE.2022.9120025.

132 L. Wu and Y. Dong, *Energy Storage Mater.*, 2021, **41**, 715–737.

133 J. Zheng, Q. Zhao, T. Tang, J. Yin, C. D. Quilty, G. D. Renderos, X. Liu, Y. Deng, L. Wang, D. C. Bock, C. Jaye, D. Zhang, E. S. Takeuchi, K. J. Takeuchi, A. C. Marschilok and L. A. Archer, *Science*, 2019, **366**, 645–648.

134 X. Zhang, J. Li, D. Liu, M. Liu, T. Zhou, K. Qi, L. Shi, Y. Zhu and Y. Qian, *Energy Environ. Sci.*, 2021, **14**, 3120–3129.

135 J. Hao, X. Li, S. Zhang, F. Yang, X. Zeng, S. Zhang, G. Bo, C. Wang and Z. Guo, *Adv. Funct. Mater.*, 2020, **30**, 2001263.

136 P. Chen, X. Yuan, Y. Xia, Y. Zhang, L. Fu, L. Liu, N. Yu, Q. Huang, B. Wang, X. Hu, Y. Wu and T. van Ree, *Adv. Sci.*, 2021, **8**, 2100309.

137 D. Lee, H. I. Kim, W. Y. Kim, S. K. Cho, K. Baek, K. Jeong, D. B. Ahn, S. Park, S. J. Kang and S. Y. Lee, *Adv. Funct. Mater.*, 2021, **31**, 2103850.

138 F. Zhang, C. Wang, J. Pan, F. Tian, S. Zeng, J. Yang and Y. Qian, *Mater. Today Energy*, 2020, **17**, 100443.

139 Z. Cao, X. Zhu, D. Xu, P. Dong, M. O. L. Chee, X. Li, K. Zhu, M. Ye and J. Shen, *Energy Storage Mater.*, 2021, **36**, 132–138.

140 A. P. Côté, A. I. Benin, N. W. Ockwig, M. O'Keeffe, A. J. Matzger and O. M. Yaghi, *Science*, 2005, **310**, 1166–1170.

141 Z. Zhao, R. Wang, C. Peng, W. Chen, T. Wu, B. Hu, W. Weng, Y. Yao, J. Zeng, Z. Chen, P. Liu, Y. Liu, G. Li, J. Guo, H. Lu and Z. Guo, *Nat. Commun.*, 2021, **12**, 6606.

142 J. H. Park, M.-J. Kwak, C. Hwang, K.-N. Kang, N. Liu, J.-H. Jang and B. A. Grzybowski, *Adv. Mater.*, 2021, **33**, 2101726.

143 J. Zhao, Y. Ying, G. Wang, K. Hu, Y. D. Yuan, H. Ye, Z. Liu, J. Y. Lee and D. Zhao, *Energy Storage Mater.*, 2022, **48**, 82–89.

144 C. Guo, J. Zhou, Y. Chen, H. Zhuang, Q. Li, J. Li, X. Tian, Y. Zhang, X. Yao, Y. Chen, S.-L. Li and Y.-Q. Lan, *Angew. Chem., Int. Ed.*, 2022, **12**, 6606.

145 R. Zhao, Y. Yang, G. Liu, R. Zhu, J. Huang, Z. Chen, Z. Gao, X. Chen and L. Qie, *Adv. Funct. Mater.*, 2021, **31**, 2001867.

146 M. Liu, L. Yang, H. Liu, A. Amine, Q. Zhao, Y. Song, J. Yang, K. Wang and F. Pan, *ACS Appl. Mater. Interfaces*, 2019, **11**, 32046–32051.

147 X. Pu, B. Jiang, X. Wang, W. Liu, L. Dong, F. Kang and C. Xu, *Nanomicro Lett.*, 2020, **12**, 152.

148 P. Zou, R. Zhang, L. Yao, J. Qin, K. Kisslinger, H. Zhuang and H. L. Xin, *Adv. Energy Mater.*, 2021, **11**, 2100982.

149 X. Jia, C. Liu, Z. G. Neale, J. Yang and G. Cao, *Chem. Rev.*, 2020, **120**, 7795–7866.

150 L. Wang, Y. Zhang, H. Hu, H.-Y. Shi, Y. Song, D. Guo, X.-X. Liu and X. Sun, *ACS Appl. Mater. Interfaces*, 2019, **11**, 42000–42005.

151 G. Yang, J. Huang, X. Wan, B. Liu, Y. Zhu, J. Wang, O. Fontaine, S. Luo, P. Hiralal, Y. Guo and H. Zhou, *EcoMat*, 2022, **4**, e12165.

152 S. Huang, L. Hou, T. Li, Y. Jiao and P. Wu, *Adv. Mater.*, 2022, **34**, 2110140.

153 C. Zhang, J. Holoubek, X. Wu, A. Daniyar, L. Zhu, C. Chen, D. P. Leonard, I. A. Rodríguez-Pérez, J.-X. Jiang, C. Fang and X. Ji, *Chem. Commun.*, 2018, **54**, 14097–14099.

154 L. Cao, D. Li, F. A. Soto, V. Ponce, B. Zhang, L. Ma, T. Deng, J. M. Seminario, E. Hu, X.-Q. Yang, P. B. Balbuena and C. Wang, *Angew. Chem., Int. Ed.*, 2021, **60**, 18845–18851.

155 L. Cao, D. Li, E. Hu, J. Xu, T. Deng, L. Ma, Y. Wang, X. Q. Yang and C. Wang, *J. Am. Chem. Soc.*, 2020, **142**, 21404–21409.

156 Z. Peng, Q. Wei, S. Tan, P. He, W. Luo, Q. An and L. Mai, *Chem. Commun.*, 2018, **54**, 4041–4044.

157 H. Qiu, X. Du, J. Zhao, Y. Wang, J. Ju, Z. Chen, Z. Hu, D. Yan, X. Zhou and G. Cui, *Nat. Commun.*, 2019, **10**, 5374.

158 H. Dong, J. Li, J. Guo, F. Lai, F. Zhao, Y. Jiao, D. J. L. Brett, T. Liu, G. He and I. P. Parkin, *Adv. Mater.*, 2021, **33**, 2007548.

159 J. Hao, L. Yuan, C. Ye, D. Chao, K. Davey, Z. Guo and S.-Z. Qiao, *Angew. Chem., Int. Ed.*, 2021, **60**, 7366–7375.

160 S.-J. Zhang, J. Hao, D. Luo, P.-F. Zhang, B. Zhang, K. Davey, Z. Lin and S.-Z. Qiao, *Adv. Energy Mater.*, 2021, **11**, 2102010.

161 T. C. Li, Y. Lim, X. L. Li, S. Luo, C. Lin, D. Fang, S. Xia, Y. Wang and H. Y. Yang, *Adv. Energy Mater.*, 2022, **12**, 2103231.

162 W. Chen, S. Guo, L. Qin, L. Li, X. Cao, J. Zhou, Z. Luo, G. Fang and S. Liang, *Adv. Funct. Mater.*, 2022, **32**, 2112609.

163 M. S. Gonzalez, Q. Yan, J. Holoubek, M. Li, Z. Wu, H. Zhou, S. Kim, H. Liu, B. Y. Jung, S. W. Lee, Z. Chen and P. Liu, *Adv. Funct. Mater.*, 2021, **31**, 2102198.

164 X. Guo, Z. Zhang, J. Li, N. Luo, G.-L. Chai, T. S. Miller, F. Lai, P. Shearing, D. J. L. Brett, D. Han, Z. Weng, G. He and I. P. Parkin, *ACS Energy Lett.*, 2021, **6**, 395–403.

165 X. Zeng, J. Mao, J. Hao, J. Liu, S. Liu, Z. Wang, Y. Wang, S. Zhang, T. Zheng, J. Liu, P. Rao and Z. Guo, *Adv. Mater.*, 2021, **33**, 2007416.

166 Y. Liu, J. Hu, Q. Lu, M. Hantusch, H. Zhang, Z. Qu, H. Tang, H. Dong, O. G. Schmidt, R. Holze and M. Zhu, *Energy Storage Mater.*, 2022, **47**, 98–104.

167 C. Sun, C. Wu, X. Gu, C. Wang and Q. Wang, *Nanomicro Lett.*, 2021, **13**, 89.

168 C. Huang, X. Zhao, Y. Hao, Y. Yang, Y. Qian, G. Chang, Y. Zhang, Q. Tang, A. Hu and X. Chen, *Adv. Funct. Mater.*, 2022, **32**, 2112091.

169 Y. An, Y. Tian, K. Zhang, Y. Liu, C. Liu, S. Xiong, J. Feng and Y. Qian, *Adv. Funct. Mater.*, 2021, **31**, 2101886.

170 Y. Chu, S. Zhang, S. Wu, Z. Hu, G. Cui and J. Luo, *Energy Environ. Sci.*, 2021, **14**, 3609–3620.

171 Y. Lv, Y. Xiao, L. Ma, C. Zhi and S. Chen, *Adv. Mater.*, 2022, **34**, 2106409.

172 C. Liu, X. Xie, B. Lu, J. Zhou and S. Liang, *ACS Energy Lett.*, 2021, **6**, 1015–1033.

173 J. Yang, B. Yin, Y. Sun, H. Pan, W. Sun, B. Jia, S. Zhang and T. Ma, *Nanomicro Lett.*, 2022, **14**, 42.

174 J. Zhu, M. Yao, S. Huang, J. Tian and Z. Niu, *Angew. Chem., Int. Ed.*, 2020, **59**, 16480–16484.

175 P. Yang, C. Feng, Y. Liu, T. Cheng, X. Yang, H. Liu, K. Liu and H. J. Fan, *Adv. Energy Mater.*, 2020, **10**, 2002898.

176 X. Lin, C. Chu, Z. Li, T. Zhang, J. Chen, R. Liu, P. Li, Y. Li, J. Zhao, Z. Huang, X. Feng, Y. Xie and Y. Ma, *Nano Energy*, 2021, **89**, 106351.

177 Z. Lei, J. Shen, J. Wang, Q. Qiu, G. Zhang, S.-S. Chi, H. Xu, S. Li, W. Zhang, Y. Zhao, Y. Deng and C. Wang, *Chem. Eng. J.*, 2021, **412**, 128733.

178 X. C. Chen, Y. Zhang, L. C. Merrill, C. Soulen, M. L. Lehmann, J. L. Schaefer, Z. Du, T. Saito and N. J. Dudney, *J. Mater. Chem. A*, 2021, **9**, 6555–6566.

179 D. Wang, X. Guo, Z. Chen, Y. Zhao, Q. Li and C. Zhi, *ACS Appl. Mater. Interfaces*, 2022, **14**, 27287–27293.

180 M. Wang, A. Emre, S. Tung, A. Gerber, D. Wang, Y. Huang, V. Cecen and N. A. Kotov, *ACS Nano*, 2019, **13**, 1107–1115.

181 Y. Zeng, X. Zhang, Y. Meng, M. Yu, J. Yi, Y. Wu, X. Lu and Y. Tong, *Adv. Mater.*, 2017, **29**, 1700274.

182 L. Ma, S. Chen, H. Li, Z. Ruan, Z. Tang, Z. Liu, Z. Wang, Y. Huang, Z. Pei, J. A. Zapien and C. Zhi, *Energy Environ. Sci.*, 2018, **11**, 2521–2530.

183 Z. Liu, Q. Yang, D. Wang, G. Liang, Y. Zhu, F. Mo, Z. Huang, X. Li, L. Ma, T. Tang, Z. Lu and C. Zhi, *Adv. Energy Mater.*, 2019, **9**, 1902473.

184 F. Mo, G. Liang, Q. Meng, Z. Liu, H. Li, J. Fan and C. Zhi, *Energy Environ. Sci.*, 2019, **12**, 706–715.

185 H. Li, C. Han, Y. Huang, Y. Huang, M. Zhu, Z. Pei, Q. Xue, Z. Wang, Z. Liu, Z. Tang, Y. Wang, F. Kang, B. Li and C. Zhi, *Energy Environ. Sci.*, 2018, **11**, 941–951.

186 Y. Huang, M. Zhong, F. Shi, X. Liu, Z. Tang, Y. Wang, Y. Huang, H. Hou, X. Xie and C. Zhi, *Angew. Chem., Int. Ed.*, 2017, **56**, 9141–9145.

187 Z. Pei, Z. Yuan, C. Wang, S. Zhao, J. Fei, L. Wei, J. Chen, C. Wang, R. Qi, Z. Liu and Y. Chen, *Angew. Chem., Int. Ed.*, 2020, **59**, 4793–4799.

188 Y. Tang, X. Li, H. Lv, D. Xie, W. Wang, C. Zhi and H. Li, *Adv. Energy Mater.*, 2020, **10**, 2000892.

189 F. Mo, Z. Chen, G. Liang, D. Wang, Y. Zhao, H. Li, B. Dong and C. Zhi, *Adv. Energy Mater.*, 2020, **10**, 2000035.

190 Z. Wang, H. Li, Z. Tang, Z. Liu, Z. Ruan, L. Ma, Q. Yang, D. Wang and C. Zhi, *Adv. Funct. Mater.*, 2018, **28**, 1804560.

191 J. Gao, X. Xie, S. Liang, B. Lu and J. Zhou, *Nanomicro Lett.*, 2021, **13**, 69.